Cosmological prior for the J-factor estimation of dwarf spheroidal galaxies

Horigome, S.; Hayashi, K.; Ando, S.

DOI
10.1103/PhysRevD.108.083530
Publication date
2023
Document Version
Final published version
Published in
Physical Review D

Cosmological prior for the *J*-factor estimation of dwarf spheroidal galaxies

Shun'ichi Horigome,[1] Kohei Hayashi,[2,3,4] and Shin'ichiro Ando[5,1]
[1]*Kavli IPMU (WPI), UTIAS, University of Tokyo, Kashiwa, Chiba, 277-8583, Japan*
[2]*National Institute of Technology, Sendai College, 48 Nodayama, Medeshima-Shiote, Natori, Miyagi 981-1239, Japan*
[3]*Astronomical Institute, Tohoku University, 6-3 Aoba, Aramaki, Aoba-ku, Sendai, Miyagi 980-8578, Japan*
[4]*Institute for Cosmic Ray Research, The University of Tokyo, Chiba, 277-8582, Japan*
[5]*GRAPPA Institute, Institute of Physics, University of Amsterdam, 1098 XH Amsterdam, The Netherlands*

(Received 31 October 2022; accepted 8 September 2023; published 27 October 2023)

Dark matter halos of dwarf spheroidal galaxies (dSphs) play important roles in dark matter detection. Generally we estimate the halo profile using a kinematical equation of dSphs but the halo profile has a large uncertainty because we have only a limited number of kinematical datasets. In this paper, we utilize cosmological models of dark matter subhalos to obtain better constraints on halo profile of dSphs. The constraints are realized as two cosmological priors: satellite prior, based on a semianalytic model of the accretion history of subhalos and their tidal stripping effect, and stellar-to-halo mass relation prior, which estimates halo mass of a galaxy from its stellar mass using empirical correlations. In addition, we adopt a radial dependent likelihood function by considering the velocity dispersion profile, which allows us to mitigate the parameter degeneracy in the previous analysis using a radial independent likelihood function with averaged dispersion. Using these priors, we estimate the squared dark matter density integrated over the region of interest (so-called J factor) of eight classical and 27 ultrafaint dSphs. Our method significantly decreases the uncertainty of J factors (up to about 20%) compared to the previous radial independent analysis. We confirm the model dependence of J-factor estimates by evaluating Bayes factors of different model setups and find that the estimates are still stable even when assuming different cosmological models.

DOI: 10.1103/PhysRevD.108.083530

I. INTRODUCTION

The presence of dark matter in our Universe is one of the most important open questions in the current physics. Even though cosmological observations agree with predictions of the Λ-cold dark matter model with surprising accuracy [1], we still do not know what dark matter is. In order to answer this question, many candidates and detection methods have been proposed [2]. Among various detection methods, those using dwarf spheroidal galaxies (dSphs) are interesting. DSphs are a kind of satellite galaxy of the Milky Way with large mass-to-light ratio, which implies that they are dark matter rich objects. Such a large amount of dark matter enables us to explore the nature of dark matter. In the indirect detection method, we can constrain the annihilation cross section by observing the signal flux of annihilation products. This method is very useful to detect well-motivated dark matter candidates such as the weakly interacting massive particles [3,4], because they have a large annihilation cross section thanks to a nonrelativistic quantum effect, so-called the Sommerfeld effect [5,6]. The sensitivity of the detection depends on the estimated amount of signal flux. This amount is proportional to an astrophysical quantity, so-called J factor:

$$J(\Delta\Omega) \equiv \int \mathrm{d}\Omega \int \mathrm{d}l \rho^2(r), \tag{1}$$

where Ω is the solid angle, $\Delta\Omega$ is the region of interest, l denotes the line-of-sight distance, r is the radius from the center of a target dSph, and $\rho(r)$ denotes the dark matter density profile. In order to obtain reliable and useful results, we need to know the accurate and precise value of the J factor, that is, the shape of dark matter density profile $\rho(r)$.

Although dSphs are useful tools to study the dark matter, their dark matter density profiles have large astrophysical uncertainty compared to other uncertainties from particle physics models. Generally, the dark matter density profile is estimated by fitting the spectroscopic dataset of dSph member stars using the Jeans equation [7]. However, the stellar dataset cannot completely determine the dark matter profile because we generally use empirical models of the dark matter profile through the fitting and their parameters are degenerated. Fortunately, from the viewpoint of cosmology, structure formation models predict the distribution of dSph profiles in the Universe, which is useful to select theoretically favored density profile model parameters and mitigate the problematic degeneracy. For instance, Ref. [8]

uses the conventional theory of spherical collapse to roughly constrain the parameter space of the dark matter density profile.

Recently, semianalytic models of the tidal mass stripping effect on the cold dark matter halo were developed [9,10], which allows us to construct a multivariate distribution of dSph mass and its tidal truncation radius. This probability distribution was applied as a prior (called *satellite prior*) for the J-factor estimation of dSphs by fitting their averaged velocity dispersion [11] and it was shown that the satellite prior has a potential to break the degeneracy among parameters of the Navarro–Frenk–White (NFW) profile [12].

While the satellite prior gives a statistical trend for the whole dSph, cosmology offers us another way to constrain the dark matter mass of an individual dSph. Since the dark matter plays an essential role in forming the structure of the Universe including dSphs, the stellar components of dSphs have a strong relation to their dark matter halo, known as the stellar-to-halo mass relation (SHMR) [13]. The dark matter halo mass in each dSph can be therefore constrained by its stellar mass by using this relation.

In this paper, we perform a more detailed analysis of the satellite prior in Ref. [11] (hereafter SA20) by considering the radial dependence of the velocity dispersion to optimize given kinematical datasets. The radial dependency weakens the degeneracy among dark matter halo parameters and gives more precise estimation than the radial independent analysis. Moreover, we consider some SHMR models to obtain more reasonable estimation results from the viewpoint of cosmology. These models help us to obtain more accurate constraints of the halo parameters than the previous satellite prior only analysis. From the other point of view, our analysis also provides a method for evaluating the credibility of each SHMR model using dark matter halos of dSphs. This paper is organized as follows: In Sec. II, we discuss our analysis method. In Sec. II A, we describe our model setups and assumptions on the dSph system and introduce our likelihood function. In Sec. II B, we explain the construction of the satellite prior and the stellar-to-halo mass relation prior. We set up several choices of these priors reflecting the uncertainty of cosmological models. In Sec. II C, we show the table of dSphs including their half-light radii and distances. The kinematical dataset and preanalysis method for each dSph is also described. In Sec. III, we show results of the analysis and estimated J-factor values. Here we compare results of different priors to verify the stability of the estimated J factor by changing cosmological models. In Sec. V, we discuss and summarize our results.

II. METHOD

A. Models and likelihood

We assume that dSphs are spherical and steady systems according to conventional analyses [8,14,16]. Their velocity dispersions are determined by the spherical Jeans equation,

$$\frac{1}{\nu(r)}\frac{\partial(\nu(r)\sigma_r^2(r))}{\partial r}+2\sigma_r^2(r)\beta(r)=-\frac{GM(r)}{r^2}, \quad (2)$$

where G is the gravitational constant, r denotes the distance from the dSph center, $\nu(r)$ is the stellar number density and $M(r)$ denotes the dark matter mass enclosed within the radius r. The anisotropy of the stellar motion $\beta(r)$ is defined by the ratio of the velocity dispersions $\sigma_r^2(r)$, $\sigma_\theta^2(r)$ and $\sigma_\phi^2(r)$ as $\beta(r)\equiv 1-\frac{\sigma_\theta^2+\sigma_\phi^2}{2\sigma_r^2}$. By definition, $\beta(r)$ satisfies $-\infty<\beta(r)\leq 1$. In this paper, we assume that $\beta(r)=\beta_{\rm ani}(\text{const})$ for simplicity.

We describe the stellar profile $\nu(r)$ as the Plummer profile, a widely used fitting function of the stellar number density of dSphs [17,18]. Its stellar number density $\nu(r)$ and surface density $\Sigma(R)$ are given by

$$\nu(r)=\frac{3}{4\pi R_e^3}\left(1+\left(\frac{r}{R_e}\right)^2\right)^{-5/2}, \quad (3)$$

$$\Sigma(R)=\frac{1}{\pi R_e^2}\left(1+\frac{R^2}{R_e^2}\right)^{-2}, \quad (4)$$

where R denotes the radius projected on the celestial sphere and R_e is the half-light radius of the surface density profile.

For the dark matter density profile, there are many discussions and no consensus exists yet. This is known as the core-cusp problem [21]; N-body simulation shows the cuspy dark matter density profile ($\rho(r)\propto r^{-1}$ around the center), while observations suggest the cored profile [$\rho(r)\propto$ const]. In this paper, we assume the cold dark matter model, then the dark matter density profile can be well described by the truncated NFW profile [12], whose mass density $\rho(r)$ and enclosed mass $M(r)\equiv\int \mathrm{d}r 4\pi r^2\rho(r)$ are respectively written as

$$\rho(r)=\begin{cases}\rho_s\left(\frac{r}{r_s}\right)^{-1}\left(1+\frac{r}{r_s}\right)^{-2} & (0\leq r\leq r_t)\\ 0 & (r_t<r),\end{cases} \quad (5)$$

$$M(r)=\begin{cases}4\pi\rho_s r_s^3 f_{\rm NFW}(r/r_s) & (0\leq r\leq r_t)\\ 4\pi\rho_s r_s^3 f_{\rm NFW}(r_t/r_s) & (r_t<r),\end{cases} \quad (6)$$

where ρ_s and r_s is scale density and radius of the profile, respectively, r_t denotes the truncation radius, and an auxiliary function $f_{\rm NFW}(x)$ is defined as follows:

$$f_{\rm NFW}(x)=\ln(1+x)-\frac{1}{1+x^{-1}}. \quad (7)$$

Using these quantities, we define our likelihood function as follows:

$$\mathcal{L}(\Theta) = \prod_i \mathcal{N}[v_i; v_{\rm dSph}, \sigma^2_{\rm los}(R_i) + \delta\sigma_i^2], \tag{8}$$

where $v_{\rm dSph}$ is the systemic velocity of each dSph, $\Theta \equiv R_e, r_s, \rho_s, r_t, \beta_{\rm ani}, v_{\rm dSph}$ represents the parameter set in our model, $\mathcal{N}[x;\mu,\sigma^2]$ denotes the normal (Gaussian) distribution with the mean μ and the variance σ^2, v_i is the observed velocity of the ith star and $\delta\sigma_i$ is its observational error. The function $\sigma^2_{\rm los}(R)$ is the projected velocity dispersion along the line of sight at projected radius R, given by the following formula:

$$\sigma^2_{\rm los}(R) = \frac{2}{\Sigma(R)} \int_R^\infty {\rm d}r \left(1 - \beta(r)\frac{R^2}{r^2}\right) \frac{\nu(r)\sigma_r^2(r)}{\sqrt{1 - R^2/r^2}}. \tag{9}$$

When $\beta(r) = \beta_{\rm ani}({\rm const})$, Eq. (9) is simplified to [22]

$$\sigma^2_{\rm los}(R) = \frac{1}{\Sigma(R)} \int_R^\infty {\rm d}s \nu(s) \frac{GM(s)}{s} K(s/R), \tag{10}$$

$$K(u) = \sqrt{1 - u^{-2}} \times \left[u^2\left(\frac{3}{2} - \beta_{\rm ani}\right) {}_2F_1\left(1, \frac{3}{2} - \beta_{\rm ani}; \frac{3}{2}; 1 - u^2\right) - \frac{1}{2}\right], \tag{11}$$

where ${}_2F_1(a,b;c;z)$ is the Gaussian hypergeometric function.

We note that our likelihood function has R dependence in contrast with that SA20 used the averaged (R-independent) velocity dispersion $\overline{\sigma^2_{\rm los}} = \frac{4\pi G}{3}\int_0^\infty {\rm d}r r\nu(r)M(r)$. The advantage of the our R-dependent analysis is that it weakens the degeneracy between parameters by probing the shape of $\sigma^2_{\rm los}(R)$ even when $\overline{\sigma^2_{\rm los}}$ is not changed.

B. Priors

1. Photometry prior

The half-light radius R_e is constrained by the result of photometric observations, which is realized as a photometric prior. We adopt a log-normal distribution for the half-light radius to construct the prior as follows:

$$\pi_{\rm photo}(\log_{10}R_e/({\rm pc})) = \mathcal{N}(\log_{10}R_e/({\rm pc})|\log_{10}r_{e,{\rm circ}}/({\rm pc}), \delta\log_{10}r_{e,{\rm circ}}/({\rm pc})), \tag{12}$$

where we calculate the mean $\log_{10} r_{e,{\rm circ}}$ and standard deviation $\delta\log_{10} r_{e,{\rm circ}}$ based on the error propagation law by using $\hat{\theta}$ listed in Table I on the supplement material of SA20 [23].

TABLE I. The half-light radius, distance from Earth, stellar mass and reference list for the 27 ultrafaint dSphs analyzed in this paper. We derive the half-light radius and its error based on the value in SA20. The values of distance and stellar mass are from SA20 and Ref. [24], respectively (see text for more details). The last column shows the source of kinematical dataset.

Name	$\log_{10}R_e/({\rm pc})$	D_* (kpc)	$M_*(M_\odot)$	Refs.
Aquarius 2	2.09 ± 0.08	108	4.7×10^3	[25]
Boötes 1	2.20 ± 0.02	66	2.9×10^4	[26]
Boötes 2	1.52 ± 0.07	42	1.0×10^3	[27,28]
CanesVenatici 1	2.53 ± 0.02	218	2.3×10^5	[29]
CanesVenatici 2	1.73 ± 0.09	160	7.9×10^3	[29]
Carina 2	1.87 ± 0.05	36	5.4×10^3	[30]
ComaBerenices	1.76 ± 0.03	44	3.7×10^3	[29]
Draco 2	1.12 ± 0.18	20	1.0×10^3	[31]
Eridanus 2	2.20 ± 0.05	380	6.5×10^4	[32]
Grus 1	1.27 ± 0.46	120	2.1×10^3	[33]
Hercules	2.08 ± 0.04	132	3.7×10^4	[29]
Horologium 1	1.49 ± 0.10	79	2.2×10^3	[34]
Hydrus 1	1.73 ± 0.03	28	6.5×10^3	[35]
Leo 4	2.01 ± 0.05	154	1.9×10^4	[29,36]
Leo T	2.13 ± 0.05	417	1.4×10^5	[29]
Leo 5	1.57 ± 0.18	178	1.1×10^4	[36]
Pegasus 3	1.62 ± 0.16	215	3.6×10^3	[37]
Pisces 2	1.68 ± 0.07	182	8.6×10^3	[38]
Reticulum 2	1.49 ± 0.02	30	3.0×10^3	[39]
Segue 1	1.30 ± 0.06	23	3.4×10^2	[40]
Segue 2	1.53 ± 0.04	35	8.6×10^2	[41]
Triangulum 2	1.10 ± 0.13	30	4.5×10^2	[42]
Tucana 2	2.21 ± 0.07	57	2.8×10^3	[33]
Tucana 3	1.64 ± 0.06	25	7.9×10^2	[43]
UrsaMajor 1	2.18 ± 0.02	97	1.4×10^4	[29]
UrsaMajor 2	1.93 ± 0.02	32	4.1×10^3	[29]
Willman 1	1.30 ± 0.05	38	1.0×10^3	[44]

2. Satellite prior

Structure formation models of subhalos in the Milky Way predict structural parameters of subhalo profile $\rho(r)$: r_s, ρ_s and r_t. In this paper we use the satellite prior proposed in SA20, briefly reviewed in the following: The formation of subhalos is well described by the extended Press-Schechter formalism [45], which gives the differential number of accreted subhalos $\frac{{\rm d}^2N_{\rm sh}}{{\rm d}z_a {\rm d}m_a}$. Here $N_{\rm sh}$ denotes the number of the subhalo, and z_a and m_a are the redshift and mass of a subhalo when the subhalo accreted onto its host. Here m_a can be reinterpreted as halo parameters $\rho_{s,a}$, $r_{s,a}$ and r_{200} by considering two conditions: (i) The subhalo is virialized $m_a = 4\pi\rho_{\rm crit}(z_a)200r^3_{200}/3$, where the virial radius r_{200} is calculated from $r_{s,a}$ by using the concentration parameter $c_a = r_{s,a}/r_{200}$, whose probability density

distribution $P(c_a)$ is given by the log-normal distribution with mean $c_{200}(m_a, z_a)$ [46] and standard deviation $\sigma_{\ln c} = 0.13$ [47]. (ii) The dark matter distribution of the subhalo is given by the NFW profile $m_{200} = 4\pi\rho_{s,a} r_s^3 f_{\rm NFW}(r_{200}/r_{s,a})$, where $f_{\rm NFW}$ is the same as defined in Eq. (7).

After the accretion, the tidal force of the Milky Way starts stripping subhalo mass. In a semianalytic strategy, the mass-loss rate through this process is modeled as

$$\frac{{\rm d}m}{{\rm d}t} = -A\frac{m(z)}{\tau_{\rm dyn}(z)}\left[\frac{m(z)}{M(z)}\right]^{\zeta}, \tag{13}$$

where $\tau_{\rm dyn}(z)$ denote the dynamical timescale [48], $m(z)$ and $M(z)$ are subhalo and host halo mass at redshift z, respectively. [Here we assume that $M(z=0) = 10^{12} M_\odot$ according to SA20. We discuss the impact of the host halo mass dependence on the prior distribution in Appendix A.] The two parameters A and ζ are calibrated by the results of N-body simulations. The solution of this equation with the initial condition $m(z_a) = m_a$ gives current $(z=0)$ subhalo mass $m_0 = m(0)$. As the subhalo mass evolves, structural parameters $\rho_{s,a}$ and $r_{s,a}$ also evolve to $\rho_{s,0}$ and $r_{s,0}$ (or simply ρ_s and r_s) according to the empirical fitting formula [47]. Finally, current truncation radius $r_{t,0}$ (or simply r_t) is determined by the NFW condition $m_0 = 4\pi\rho_{s,0} r_{s,0}^3 f_{\rm NFW}(r_{t,0}/r_{s,0})$.

We combine the two distributions of parameters at accretion $\frac{{\rm d}^2 N_{\rm sh}}{{\rm d}z_a {\rm d}m_a}$ and $P(c_a)$ with the parameter evolution model to obtain the distribution of parameters at present [49]. Instead of calculating the distribution of current parameters directly by using the Jacobian of the evolution formula, we obtain finite samples of the parameters. We subdivide $(\ln m_a, z_a, c_a)$ linearly and calculate the weight of the ith grid according to

$$w_i = N\left.\frac{{\rm d}^2 N_{\rm sh}}{{\rm d}z_a {\rm d}m_a}\right|_{z_a = z_{a,i}, m_a = m_{a,i}} (\Delta z_a)_i (\Delta m_a)_i \times P(c_a)|_{c_a = c_{a,i}} (\Delta c_a)_i, \tag{14}$$

where N is a normalization factor to satisfy the condition $\sum_i w_i = N_{\rm sh,tot} \equiv \iint {\rm d}z_a {\rm d}m_a \frac{{\rm d}^2 N_{\rm sh}}{{\rm d}z_a {\rm d}m_a}$. Each point $(\ln m_{a,i}, z_{a,i}, c_{a,i})$ is interpreted to $(\rho_{s,i}, r_{s,i}, c_{t,i})$ according to the stripping model, then we obtain finite samples of (ρ_s, r_s, c_t) with its weight [50].

Some subhalos do not host any stars because baryons in too small of a halo cannot lose their energy due to its ionizing background, known as reionization suppression [51,52]. In order to consider the effect, we multiply w_i by the formation probability of a satellite for the given subhalo $P_{\rm form}$ as follows:

$$P_{\rm form}(V_{\rm peak}) = \frac{1}{2}\left[1 + {\rm erf}\left(\frac{V_{\rm peak} - V_{50}}{\sqrt{2}\sigma}\right)\right], \tag{15}$$

where $V_{\rm peak}$ denotes the maximum circular velocity of the satellite at accretion time, given by $V_{\rm peak} = (4\pi G\rho_{s,a}/4.625)^{1/2} r_{s,a}$ for a NFW subhalo and it is calculated for each parameter grid $(\rho_{s,i}, r_{s,i}, c_{t,i})$. For the lower bound parameter V_{50}, we have two choices: $V_{50} = 18$ km/s, motivated by conventional theory of reionization [53–56], and $V_{50} = 10.5$ km/s, based on the result of more resent analysis [52]. For σ, we adopt $\sigma = 2.5\ {\rm km\,s^{-1}}$, following Ref. [52]. For classical dSphs, we adopt $V_{50} = 25$ km/s according to [57]. Here we assume $\sigma = 0\ {\rm km\,s^{-1}}$ for simplicity. In this case $P_{\rm form}(V_{\rm peak})$ is equivalent to a step function $\Theta(V_{\rm peak} - V_{50})$.

Using these quantities, the probability density distribution of the three profile parameters is then given by

$$\pi_{\rm sat}(r_s, \rho_s, r_t) \propto \frac{{\rm d}^3 N_{\rm sh}}{{\rm d}r_s {\rm d}\rho_s {\rm d}r_t} P_{\rm form}(V_{\rm peak}), \tag{16}$$

where $\pi_{\rm sat}$. should be properly normalized to be a probability density distribution function. For the discrete sample points generated above, it is realized as

$$\pi_{\rm sat,i} = \frac{w_i P_{\rm form}(V_{{\rm peak},i})}{\sum_i w_i P_{\rm form}(V_{{\rm peak},i})}. \tag{17}$$

Finally we smooth these samples $\{\pi_{{\rm sat},i}\}$ to reconstruct a prior function $\pi_{\rm sat}(r_s, \rho_s, r_t)$ by using weighted kernel density estimation implemented in SciPy [58].

3. SHMR prior

In addition to the satellite prior, we use another prior motivated by the stellar-to-halo mass relation (SHMR) (see [59] for a review). This relation is obtained by fitting the structure formation model by using observed cosmological datasets with a simple assumption; the larger the halo becomes, the more stars it hosts. Stellar mass m_* is then written as a monotonic function of halo mass m_z for given redshift z. We identify $m(z)$ with the subhalo mass at the accretion time and relate it to the current subhalo mass using the semianalytic approach mentioned in Sec. II B 2. Here, for the simplicity, we assume that the stellar mass does not change after accretion and identify m_* as the current stellar mass [60]. The schematic figure of this procedure is shown in Fig. 1.

In order to check model dependence, we adopt four SHMR models [61–64] (hereafter PB13, BM13, PB19 and BM18, respectively). These models have the following features:

(i) PB13: calibrated by the Bolshoi simulation, using a multipower law fitting function for the SHMR and fitting the SHMR intrinsic parameters with other systematic parameters.

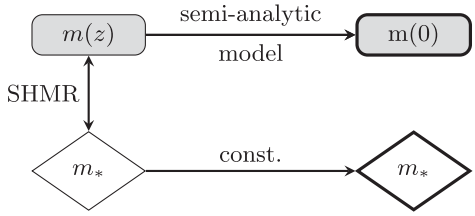

FIG. 1. A schematic picture to illustrate how to construct our SHMR prior. Horizontal one-side arrows indicate time evolution. Shapes with bold edges are values at present ($z = 0$), which appeared in the definition of the SHMR prior in Eq. (18).

(ii) BM13: calibrated by the Millennium simulation, using a double-power law fitting function for the SHMR and simply fitting SHMR parameters.
(iii) PB19: updated datasets from PB13, cosmological models calibrated by the Bolshoi-Planck simulation, using a double-power law fitting function for the SHMR and simply fitting SHMR parameters.
(iv) BM18: updated datasets from BM13, cosmological models assuming double-power law for the evolution of baryon conversion efficiency calibrated by an independent simulation, using double-power law for the SHMR and simply fitting SHMR parameters.

The probability density distribution of stellar mass m_* is given by the log-normal distribution as follows:

$$P(m_*|m(z)) = (1/m_* \ln 10)\mathcal{N}[\log_{10}(m_*/[M_\odot]); \log_{10}(m_*(m(z),z)/[M_\odot]), \delta\log_{10}(m_*/[M_\odot])], \tag{18}$$

where $m_*(M_h, z)$ is expected stellar mass for given halo mass M_h at accretion redshift z, shown in Fig. 2 for each model. $\delta\log_{10}(m_*/[M_\odot])$ denotes the model uncertainty of each SHMR model from each literature.

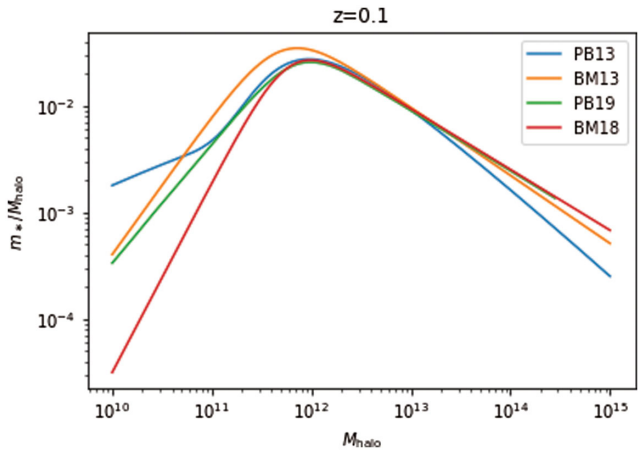

FIG. 2. SHMR function $m_*(M_h, z)$ normalized by the halo mass M_h. Here we fix $z = 0.1$ for illustration purposes.

We discuss the impact of varying the uncertainty in Appendix B since, in this analysis, we refer the low-mass end of the relation where we have few datasets to determine SHMR uncertainties.

In terms of the Bayesian statistics, we can compare credibility of a model (model 1) to a reference model (model 0) by using Bayes factor BF, defined as the ratio of Bayesian evidences $\mathcal{E}$:

$$\mathrm{BF} = \frac{\mathcal{E}_1}{\mathcal{E}_0} = \frac{\int d\Theta_1 \mathcal{L}_1(\Theta_1)\pi_1(\Theta_1)}{\int d\Theta_0 \mathcal{L}_0(\Theta_0)\pi_0(\Theta_0)}. \tag{19}$$

Here the minus logarithm of the Bayesian evidence $-\ln\mathcal{E}$ is approximated by the widely applicable Bayesian information criterion (WBIC) [65]:

$$-\ln\mathcal{E} \simeq \mathrm{WBIC} = -\frac{\int d\Theta (\ln\mathcal{L}(\Theta))\mathcal{L}(\Theta)^\beta \pi(\Theta)}{\int d\Theta \mathcal{L}(\Theta)^\beta \pi(\Theta)}, \tag{20}$$

$$\beta = 1/\ln(\#\mathrm{data}). \tag{21}$$

In this work, we calculate WBIC of each model using the Markov chain Monte Carlo algorithm and evaluate the Bayes factor according to

$$\ln \mathrm{BF} = \ln\mathcal{E}_1 - \ln\mathcal{E}_0 \simeq -\mathrm{WBIC}_1 + \mathrm{WBIC}_0. \tag{22}$$

Here $\mathrm{BF} > 1$ or $\ln\mathrm{BF} > 0$ means that model 1 is more credible than model 0. According to Ref. [66], there is a scale for interpreting $\ln\mathrm{BF}$ into the strength of evidence as follows: *Decisive* for $\ln\mathrm{BF} \gtrsim 4$, *very strong* for $3 \lesssim \ln\mathrm{BF} \lesssim 4$, *strong* for $2 \lesssim \ln\mathrm{BF} \lesssim 3$, *substantial* for $1 \lesssim \ln\mathrm{BF} \lesssim 2$, and *barely worth mentioning* for $0 \lesssim \ln\mathrm{BF} \lesssim 1$.

C. Data

We analyze the dSphs listed in Tables I and II according to SA20, where we show the half-light radius, distance, and stellar mass of each dSph. The half-light radius and distances are from SA20 and also we use the values in

TABLE II. Same as Table I, but for classical dSphs.

Name	$\log_{10}R_e/(\mathrm{pc})$	D_* (kpc)	$M_*(M_\odot)$	Refs.
Carina	2.392 ± 0.005	105	3.8×10^5	[67]
Draco	2.256 ± 0.005	76	2.9×10^5	[68]
Fornax	2.849 ± 0.003	147	2.0×10^7	[67]
Leo 1	2.353 ± 0.004	254	5.5×10^6	[69]
Leo 2	2.217 ± 0.005	233	7.4×10^5	[70]
Sculptor	2.359 ± 0.004	86	2.3×10^6	[67]
Sextans 1	2.538 ± 0.004	86	4.4×10^5	[67]
UrsaMinor	2.434 ± 0.006	76	2.9×10^5	[71]

Ref. [24] for the stellar masses. For dSphs without stellar mass values in Ref. [24], we calculate their stellar masses from apparent magnitudes and distances, assuming $M/L = 1$ according to Ref. [24]. The last column in Table I and II indicates references of the kinematical dataset. In general, the kinematical dataset includes member stars and foreground stars. For datasets having a membership flag, we extract stars identified as members. For those containing membership probability P_M, we choose memberlike stars ($P_M > 0.95$). For the other datasets having no membership information, we adopt the selection criteria illustrated and described in the reference. In addition, we remove member stars identified as binary stars in order to avoid accidental increase of the velocity dispersion.

D. Analysis

Based on the likelihood and priors defined above, we can calculate the posterior probability density distribution (or simply posterior) $P(\Theta|D)$ by using the Bayes' theorem:

$$P(\Theta|D) = \frac{\mathcal{L}(\Theta)\pi(\Theta)}{\int d\Theta \mathcal{L}(\Theta)\pi(\Theta)}, \tag{23}$$

where

$$\pi = \begin{cases} \pi_{\rm photo} & \text{(without any cosmological priors)} \\ \pi_{\rm photo}\pi_{\rm sat} & \text{(satellite prior only)} \\ \pi_{\rm photo}\pi_{\rm sat+SHMR} & \text{(satellite and SHMR prior).} \end{cases} \tag{24}$$

Here, as mentioned in Sec. II B, the satellite prior $\pi_{\rm sat}$ is selected from two candidates $\mathrm{sat}_{10.5}$ and sat_{18}, and the SHMR model for $\pi_{\rm sat+SHMR}$ is chosen from PB13, BM13, PB19 and BM18.

Instead of calculating Eq. (23) straightforwardly, we obtain samples from the posterior by using the Markov chain Monte Carlo methods. In this paper, we use the Affine invariant ensemble sampler implemented in EMCEE [72]. We scan the parameter region as shown in Table III. For R_e, r_s, ρ_s and r_t we adopt the logarithmic scale, reflecting that they are positive. The range for the anisotropy $\beta_{\rm ani}$ is set to include both of the radial and tangential cases. Since $v_{\rm dSph}$ is strongly constrained by the likelihood function, we choose its limits large enough to include the estimated value.

TABLE III. Scanning region of each parameter.

Parameter	Minimum	Maximum
$\log_{10}R_e/(\mathrm{pc})$	1.0	3.5
$\log_{10}r_s/(\mathrm{pc})$	0.0	5.0
$\log_{10}\rho_s/(M_\odot \mathrm{pc}^{-3})$	−4.0	4.0
$\log_{10}r_t/(\mathrm{pc})$	0.0	5.0
$-\log_{10}(1-\beta_{\rm ani})$	−1.0	1.0
$v_{\rm dSph}/(\mathrm{kms}^{-1})$	−1000	1000

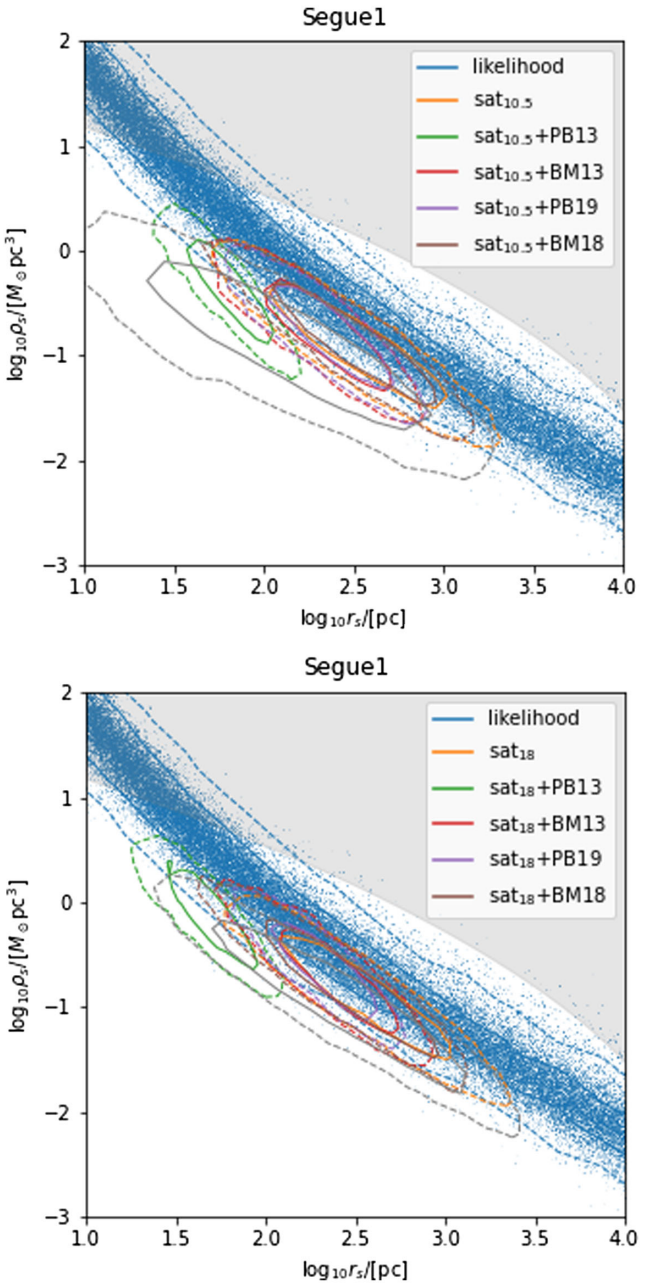

FIG. 3. Posterior probability density function projected onto the r_s-ρ_s plane for the case of Segue 1. The top and bottom panels show results assuming the $\mathrm{sat}_{10.5}$ and sat_{18} model, respectively. Blue dots are distributed according to likelihood only analysis (without any cosmological priors), while colored contours show posteriors with cosmological priors. The gray shaded area shows the cosmological constraint adopted in Ref. [8]. For the other dSphs, see Fig. 9–12.

III. RESULTS

Figure 3 shows the posterior projected onto the r_s-ρ_s plane. The value of the likelihood function is shown by blue dots and contours. Colored contours denote posteriors assuming the satellite and/or SHMR priors. The satellite prior itself is shown by gray contours and the gray shaded area shows the cosmological constraint adopted in Ref. [8].

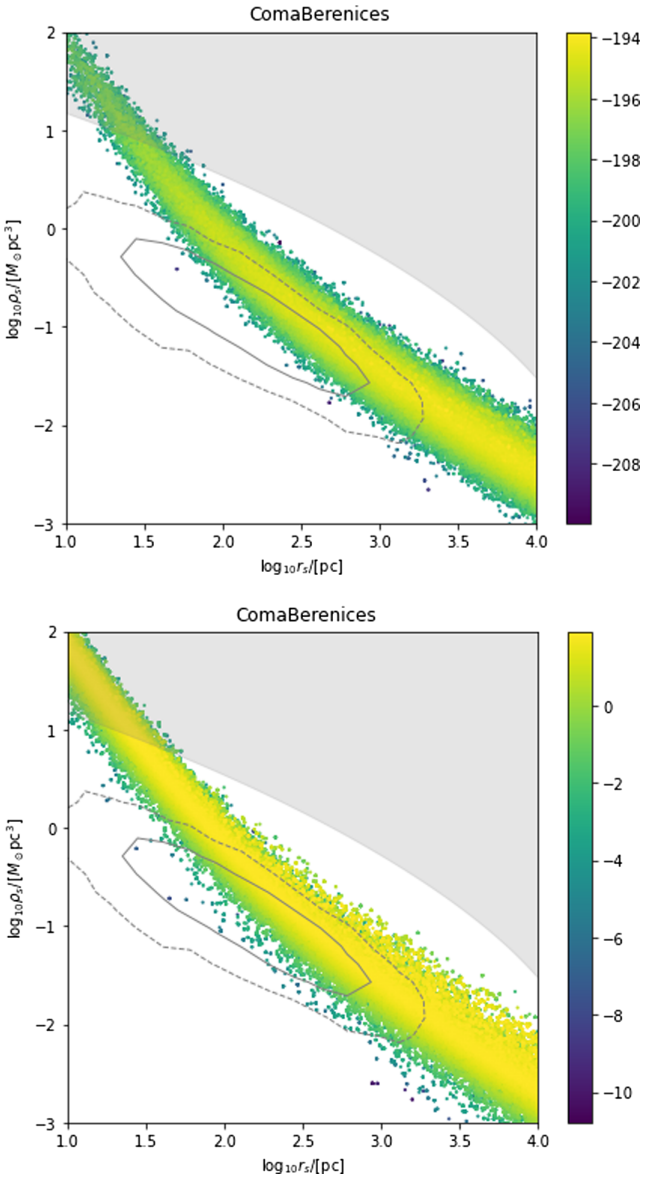

FIG. 4. Results of likelihood only (without any cosmological priors) analyses. The top panel is for the R-dependent likelihood function, [Eq. (8)], while the bottom panel is for the R-independent likelihood (see text), respectively. The color of the heat map corresponds to the value of profiled likelihood function $\mathcal{L}_{\mathrm{prof}}(r_s,\rho_s) \equiv \max_{r_t} \mathcal{L}(r_s,\rho_s,r_t)$. Gray contours denote the 1σ and 2σ regions of the satellite prior and the gray shaded region shows the rough cosmological prior adopted in Ref. [8]. For illustration purposes, we show only the Coma Berenices case. For illustration purposes, we only show the result of Segue 1. For other dSphs, see Fig. 9–12.

In order to clarify the advantage of R-dependent analysis, we compare results of R-dependent and R-independent likelihood analyses in Fig. 4, where R-independent likelihood is defined similarly to Eq. (8) but the velocity dispersion $\sigma^2_{\mathrm{los}}(R)$ is replaced by averaged dispersion $\overline{\sigma^2_{\mathrm{los}}}$. In Fig. 4 the color of the heat map corresponds to the value of likelihood functions.

Tables IV and V show the median values of J-factor posteriors with 68% ($\sim 1\sigma$) credible intervals. The left three columns show results without SHMR priors. In particular, the "flat" column denotes those without any cosmological priors (only with the likelihood and the photometry prior). The following columns are those with SHMR priors, PB13, BM13, PB19, and BM18, respectively. These results are also shown in Fig. 5. In Fig. 5, we also show the results of conventional analysis [11] as gray bars and the J-factor values adopted in the Fermi-LAT analysis [73] for comparison.

We show the Bayes factor of each model in Table VI. Column 1 shows the Bayes factor of sat_{18} to a reference model $\mathrm{sat}_{10.5}$ for each dSph. Columns 2–5 show the Bayes factors of the satellite prior $\mathrm{sat}_{10.5}$ and SHMR analyses to the satellite prior only analysis as a reference. Columns 6–9 are the same as columns 2–5 but for sat_{18} cases. Here a positive (negative) value indicates that the corresponding model is more (less) credible than $\mathrm{sat}_{10.5}$.

IV. DISCUSSION

A. Posterior

For Boötes 2, Draco 2, Leo 4, Pegesus 3, Pisces 2, Segue 2, Triangulum 2 and Tucana 3, their posterior distributions of r_s-ρ_s without satellite priors (likelihood) are broadly distributed (Fig. 9–12). This is because observational errors of spectroscopic dataset are too large to exclude the small r_s-ρ_s region (dSph without dark matter). In such a case, the GS15-like cut excludes the heavier halo mass region but the estimated J factor is still distributed broadly towards the small r_s-ρ_s region, thus the choice of scanning range of r_s and ρ_s strongly affects the result of estimation. This problem is solved by introducing the satellite prior because it excludes the small r_s-ρ_s region based on the formation history of dSphs.

For the other ultrafaint dSphs, posterior distribution becomes more ridgy thanks to a large amount of kinematical data. In contrast with those obtained in SA20, the likelihood edges become narrow towards the upper left (compact) or lower right (faint) regions, which indicates that the height of likelihood peak varies from the upper left to the lower right. This is thanks to the radial dependence of the velocity dispersion $\sigma(R)$; even though $\bar{\sigma}$ can be constant by varying r_s and ρ_s properly, $\sigma(R)$ cannot be kept to fit observed stellar velocity distribution at all radii.

TABLE IV. Median and 1σ interval of the estimated J factors. $\mathrm{sat}_{10.5}$ and sat_{18} denote the satellite prior assuming $V_{50} = 10.5$ and 18 km/s, respectively.

	w/o SHMR			PB13		BM13		PB19		BM18	
Name	flat	$\mathrm{sat}_{10.5}$	sat_{18}	$\mathrm{sat}_{10.5}$	sat_{18}	$\mathrm{sat}_{10.5}$	sat_{18}	$\mathrm{sat}_{10.5}$	sat_{18}	$\mathrm{sat}_{10.5}$	sat_{18}
Aquarius2	$18.25^{+0.61}_{-0.55}$	$17.62^{+0.37}_{-0.36}$	$17.84^{+0.35}_{-0.36}$	$17.21^{+0.26}_{-0.24}$	$17.31^{+0.26}_{-0.24}$	$17.57^{+0.31}_{-0.32}$	$17.73^{+0.34}_{-0.37}$	$17.71^{+0.31}_{-0.35}$	$17.80^{+0.31}_{-0.35}$	$17.92^{+0.34}_{-0.33}$	$17.91^{+0.33}_{-0.34}$
Bootes1	$18.24^{+0.28}_{-0.26}$	$18.03^{+0.22}_{-0.21}$	$18.11^{+0.21}_{-0.21}$	$17.95^{+0.19}_{-0.18}$	$17.99^{+0.18}_{-0.17}$	$18.09^{+0.21}_{-0.21}$	$18.09^{+0.21}_{-0.21}$	$18.12^{+0.22}_{-0.20}$	$18.12^{+0.21}_{-0.20}$	$18.31^{+0.19}_{-0.18}$	$18.30^{+0.18}_{-0.17}$
Bootes2	$16.64^{+2.80}_{-4.90}$	$17.69^{+0.65}_{-0.81}$	$18.41^{+0.46}_{-0.53}$	$17.48^{+0.28}_{-0.29}$	$17.53^{+0.32}_{-0.29}$	$17.64^{+0.53}_{-0.49}$	$17.84^{+0.69}_{-0.67}$	$17.74^{+0.58}_{-0.73}$	$18.33^{+0.39}_{-0.42}$	$18.33^{+0.41}_{-0.38}$	$18.35^{+0.44}_{-0.41}$
CanesVenatici1	$17.59^{+0.32}_{-0.19}$	$17.42^{+0.13}_{-0.12}$	$17.45^{+0.12}_{-0.12}$	$17.41^{+0.13}_{-0.12}$	$17.45^{+0.14}_{-0.12}$	$17.45^{+0.11}_{-0.11}$	$17.44^{+0.12}_{-0.12}$	$17.47^{+0.12}_{-0.12}$	$17.46^{+0.13}_{-0.12}$	$17.46^{+0.10}_{-0.07}$	$17.46^{+0.10}_{-0.07}$
CanesVenatici2	$17.94^{+0.50}_{-0.45}$	$17.40^{+0.37}_{-0.36}$	$17.58^{+0.30}_{-0.31}$	$16.98^{+0.23}_{-0.25}$	$17.08^{+0.23}_{-0.25}$	$17.38^{+0.27}_{-0.31}$	$17.48^{+0.27}_{-0.32}$	$17.47^{+0.27}_{-0.28}$	$17.51^{+0.27}_{-0.28}$	$17.68^{+0.30}_{-0.31}$	$17.68^{+0.30}_{-0.30}$
Carina2	$18.38^{+0.56}_{-0.55}$	$18.06^{+0.41}_{-0.37}$	$18.35^{+0.37}_{-0.36}$	$18.00^{+0.25}_{-0.26}$	$18.06^{+0.26}_{-0.25}$	$18.15^{+0.33}_{-0.32}$	$18.18^{+0.39}_{-0.36}$	$18.17^{+0.39}_{-0.42}$	$18.39^{+0.33}_{-0.35}$	$18.53^{+0.30}_{-0.27}$	$18.56^{+0.30}_{-0.27}$
ComaBerenices	$18.95^{+0.34}_{-0.36}$	$18.58^{+0.28}_{-0.29}$	$18.70^{+0.26}_{-0.26}$	$18.13^{+0.23}_{-0.23}$	$18.19^{+0.24}_{-0.23}$	$18.49^{+0.25}_{-0.27}$	$18.60^{+0.24}_{-0.26}$	$18.55^{+0.25}_{-0.27}$	$18.63^{+0.23}_{-0.24}$	$18.71^{+0.25}_{-0.26}$	$18.71^{+0.26}_{-0.27}$
Draco2	$16.80^{+2.54}_{-4.77}$	$18.30^{+0.62}_{-0.78}$	$18.93^{+0.43}_{-0.49}$	$18.12^{+0.29}_{-0.29}$	$18.15^{+0.29}_{-0.27}$	$18.28^{+0.49}_{-0.48}$	$18.40^{+0.69}_{-0.61}$	$18.35^{+0.54}_{-0.70}$	$18.89^{+0.37}_{-0.43}$	$18.90^{+0.37}_{-0.35}$	$18.93^{+0.38}_{-0.35}$
Eridanus2	$17.29^{+0.38}_{-0.36}$	$16.91^{+0.25}_{-0.24}$	$16.98^{+0.24}_{-0.23}$	$16.76^{+0.20}_{-0.19}$	$16.81^{+0.19}_{-0.19}$	$16.97^{+0.22}_{-0.23}$	$16.96^{+0.22}_{-0.22}$	$17.03^{+0.21}_{-0.21}$	$17.03^{+0.23}_{-0.23}$	$17.15^{+0.14}_{-0.16}$	$17.14^{+0.14}_{-0.15}$
Grus1	$17.42^{+0.88}_{-0.89}$	$17.09^{+0.46}_{-0.48}$	$17.44^{+0.44}_{-0.44}$	$16.77^{+0.26}_{-0.25}$	$16.85^{+0.28}_{-0.26}$	$17.05^{+0.42}_{-0.41}$	$17.26^{+0.46}_{-0.50}$	$17.15^{+0.41}_{-0.48}$	$17.43^{+0.36}_{-0.39}$	$17.53^{+0.37}_{-0.36}$	$17.51^{+0.39}_{-0.35}$
Hercules	$17.89^{+0.37}_{-0.37}$	$17.51^{+0.30}_{-0.27}$	$17.69^{+0.28}_{-0.27}$	$17.43^{+0.21}_{-0.21}$	$17.48^{+0.22}_{-0.23}$	$17.62^{+0.26}_{-0.27}$	$17.61^{+0.26}_{-0.25}$	$17.69^{+0.26}_{-0.29}$	$17.69^{+0.27}_{-0.28}$	$17.93^{+0.18}_{-0.20}$	$17.95^{+0.18}_{-0.21}$
Horologium1	$19.08^{+0.68}_{-0.63}$	$18.11^{+0.41}_{-0.40}$	$18.26^{+0.33}_{-0.37}$	$17.53^{+0.24}_{-0.23}$	$17.59^{+0.25}_{-0.24}$	$17.95^{+0.31}_{-0.34}$	$18.18^{+0.30}_{-0.36}$	$18.05^{+0.31}_{-0.34}$	$18.18^{+0.28}_{-0.30}$	$18.25^{+0.35}_{-0.36}$	$18.29^{+0.34}_{-0.36}$
Hydrus1	$18.52^{+0.36}_{-0.32}$	$18.33^{+0.29}_{-0.27}$	$18.50^{+0.31}_{-0.28}$	$18.25^{+0.21}_{-0.19}$	$18.30^{+0.21}_{-0.21}$	$18.37^{+0.26}_{-0.26}$	$18.38^{+0.31}_{-0.26}$	$18.42^{+0.29}_{-0.31}$	$18.51^{+0.26}_{-0.27}$	$18.69^{+0.25}_{-0.22}$	$18.68^{+0.25}_{-0.22}$
Leo4	$15.63^{+1.85}_{-5.06}$	$16.72^{+0.53}_{-0.61}$	$17.17^{+0.47}_{-0.46}$	$16.96^{+0.27}_{-0.27}$	$17.01^{+0.27}_{-0.29}$	$17.09^{+0.39}_{-0.37}$	$17.15^{+0.37}_{-0.41}$	$16.95^{+0.53}_{-0.50}$	$17.18^{+0.43}_{-0.47}$	$17.70^{+0.28}_{-0.27}$	$17.69^{+0.27}_{-0.28}$
Leo5	$17.18^{+0.78}_{-0.82}$	$16.92^{+0.45}_{-0.48}$	$17.28^{+0.36}_{-0.43}$	$16.73^{+0.27}_{-0.26}$	$16.87^{+0.26}_{-0.26}$	$17.07^{+0.34}_{-0.34}$	$17.16^{+0.37}_{-0.39}$	$17.17^{+0.36}_{-0.43}$	$17.29^{+0.32}_{-0.37}$	$17.56^{+0.30}_{-0.30}$	$17.51^{+0.33}_{-0.31}$
LeoT	$17.61^{+0.43}_{-0.44}$	$16.95^{+0.31}_{-0.31}$	$17.01^{+0.27}_{-0.29}$	$16.82^{+0.22}_{-0.22}$	$16.87^{+0.23}_{-0.23}$	$17.07^{+0.26}_{-0.29}$	$17.09^{+0.24}_{-0.28}$	$17.12^{+0.26}_{-0.30}$	$17.12^{+0.27}_{-0.32}$	$17.06^{+0.10}_{-0.12}$	$17.05^{+0.10}_{-0.14}$
Pegasus3	$17.82^{+1.01}_{-2.10}$	$16.72^{+0.60}_{-0.72}$	$17.23^{+0.44}_{-0.51}$	$16.41^{+0.29}_{-0.28}$	$16.45^{+0.31}_{-0.31}$	$16.78^{+0.46}_{-0.51}$	$17.00^{+0.50}_{-0.66}$	$16.88^{+0.47}_{-0.74}$	$17.17^{+0.35}_{-0.39}$	$17.35^{+0.39}_{-0.42}$	$17.35^{+0.39}_{-0.39}$
Pisces2	$17.24^{+0.91}_{-1.17}$	$16.74^{+0.55}_{-0.56}$	$17.15^{+0.46}_{-0.48}$	$16.70^{+0.27}_{-0.27}$	$16.72^{+0.30}_{-0.30}$	$16.87^{+0.42}_{-0.38}$	$16.94^{+0.47}_{-0.45}$	$16.93^{+0.48}_{-0.60}$	$17.15^{+0.42}_{-0.46}$	$17.47^{+0.33}_{-0.33}$	$17.50^{+0.34}_{-0.34}$
Reticulum2	$18.98^{+0.37}_{-0.36}$	$18.65^{+0.30}_{-0.30}$	$18.80^{+0.27}_{-0.28}$	$18.31^{+0.21}_{-0.20}$	$18.35^{+0.21}_{-0.20}$	$18.57^{+0.27}_{-0.28}$	$18.70^{+0.29}_{-0.32}$	$18.68^{+0.25}_{-0.28}$	$18.75^{+0.25}_{-0.26}$	$18.81^{+0.27}_{-0.27}$	$18.82^{+0.26}_{-0.27}$
Segue1	$19.74^{+0.39}_{-0.41}$	$19.20^{+0.33}_{-0.39}$	$19.32^{+0.28}_{-0.33}$	$18.22^{+0.29}_{-0.31}$	$18.36^{+0.31}_{-0.33}$	$18.95^{+0.30}_{-0.37}$	$19.23^{+0.27}_{-0.30}$	$18.98^{+0.30}_{-0.34}$	$19.21^{+0.25}_{-0.29}$	$19.20^{+0.31}_{-0.35}$	$19.23^{+0.30}_{-0.36}$
Segue2	$18.02^{+0.70}_{-2.06}$	$18.01^{+0.46}_{-0.50}$	$18.42^{+0.37}_{-0.41}$	$17.66^{+0.26}_{-0.26}$	$17.72^{+0.27}_{-0.28}$	$17.93^{+0.40}_{-0.44}$	$18.11^{+0.44}_{-0.60}$	$18.11^{+0.37}_{-0.51}$	$18.37^{+0.30}_{-0.37}$	$18.38^{+0.32}_{-0.30}$	$18.39^{+0.35}_{-0.34}$
Triangulum2	$14.36^{+2.91}_{-3.86}$	$17.75^{+0.67}_{-0.86}$	$18.54^{+0.43}_{-0.49}$	$17.56^{+0.29}_{-0.29}$	$17.63^{+0.27}_{-0.28}$	$17.68^{+0.55}_{-0.49}$	$17.96^{+0.65}_{-0.68}$	$17.77^{+0.57}_{-0.70}$	$18.44^{+0.36}_{-0.42}$	$18.43^{+0.37}_{-0.38}$	$18.39^{+0.43}_{-0.36}$
Tucana2	$18.14^{+0.58}_{-0.52}$	$17.87^{+0.38}_{-0.36}$	$18.16^{+0.36}_{-0.35}$	$17.57^{+0.26}_{-0.25}$	$17.68^{+0.25}_{-0.23}$	$17.84^{+0.33}_{-0.30}$	$18.02^{+0.36}_{-0.35}$	$17.96^{+0.33}_{-0.35}$	$18.10^{+0.32}_{-0.32}$	$18.20^{+0.32}_{-0.30}$	$18.19^{+0.32}_{-0.29}$
Tucana3	$15.71^{+1.79}_{-4.35}$	$17.52^{+0.45}_{-0.56}$	$18.06^{+0.34}_{-0.33}$	$17.73^{+0.25}_{-0.27}$	$17.80^{+0.26}_{-0.25}$	$17.63^{+0.35}_{-0.29}$	$17.65^{+0.35}_{-0.30}$	$17.53^{+0.46}_{-0.38}$	$18.05^{+0.43}_{-0.50}$	$18.29^{+0.27}_{-0.24}$	$18.25^{+0.27}_{-0.23}$
UrsaMajor1	$18.66^{+0.30}_{-0.29}$	$18.30^{+0.22}_{-0.22}$	$18.34^{+0.20}_{-0.20}$	$18.03^{+0.21}_{-0.19}$	$18.09^{+0.19}_{-0.20}$	$18.26^{+0.20}_{-0.20}$	$18.27^{+0.20}_{-0.19}$	$18.30^{+0.20}_{-0.20}$	$18.30^{+0.20}_{-0.19}$	$18.39^{+0.19}_{-0.19}$	$18.38^{+0.20}_{-0.19}$
UrsaMajor2	$19.54^{+0.38}_{-0.38}$	$19.01^{+0.29}_{-0.28}$	$19.10^{+0.25}_{-0.24}$	$18.56^{+0.23}_{-0.24}$	$18.63^{+0.24}_{-0.24}$	$18.91^{+0.26}_{-0.25}$	$19.05^{+0.25}_{-0.26}$	$18.98^{+0.25}_{-0.25}$	$19.04^{+0.25}_{-0.24}$	$19.12^{+0.26}_{-0.27}$	$19.13^{+0.27}_{-0.27}$
Willman1	$19.50^{+0.44}_{-0.44}$	$18.85^{+0.34}_{-0.38}$	$18.95^{+0.29}_{-0.34}$	$18.04^{+0.27}_{-0.28}$	$18.14^{+0.27}_{-0.30}$	$18.59^{+0.30}_{-0.32}$	$18.86^{+0.29}_{-0.32}$	$18.70^{+0.29}_{-0.33}$	$18.84^{+0.26}_{-0.28}$	$18.86^{+0.32}_{-0.33}$	$18.92^{+0.31}_{-0.35}$

TABLE V. Same as Table IV, but for classical dSphs.

	w/o SHMR		PB13	BM13	PB19	BM18
Name	flat	sat	sat	sat	sat	sat
Carina	$17.86^{+0.09}_{-0.07}$	$17.86^{+0.07}_{-0.06}$	$17.85^{+0.06}_{-0.06}$	$17.85^{+0.06}_{-0.06}$	$17.86^{+0.07}_{-0.06}$	$17.87^{+0.06}_{-0.06}$
Draco	$18.92^{+0.06}_{-0.06}$	$18.89^{+0.06}_{-0.06}$	$18.85^{+0.06}_{-0.06}$	$18.85^{+0.06}_{-0.06}$	$18.85^{+0.06}_{-0.06}$	$18.88^{+0.06}_{-0.06}$
Fornax	$17.93^{+0.20}_{-0.08}$	$18.03^{+0.11}_{-0.10}$	$18.02^{+0.10}_{-0.08}$	$18.00^{+0.09}_{-0.07}$	$18.02^{+0.09}_{-0.08}$	$17.96^{+0.07}_{-0.06}$
Leo1	$17.80^{+0.22}_{-0.14}$	$17.71^{+0.10}_{-0.09}$	$17.73^{+0.08}_{-0.08}$	$17.73^{+0.11}_{-0.09}$	$17.74^{+0.12}_{-0.09}$	$17.78^{+0.14}_{-0.11}$
Leo2	$17.82^{+0.25}_{-0.20}$	$17.70^{+0.16}_{-0.14}$	$17.64^{+0.13}_{-0.11}$	$17.69^{+0.15}_{-0.13}$	$17.71^{+0.15}_{-0.14}$	$17.73^{+0.17}_{-0.14}$
Sculptor	$18.56^{+0.07}_{-0.05}$	$18.55^{+0.04}_{-0.04}$	$18.55^{+0.04}_{-0.04}$	$18.55^{+0.04}_{-0.04}$	$18.55^{+0.05}_{-0.04}$	$18.56^{+0.04}_{-0.04}$
Sextans1	$18.09^{+0.40}_{-0.16}$	$18.12^{+0.15}_{-0.13}$	$18.09^{+0.14}_{-0.11}$	$18.09^{+0.14}_{-0.12}$	$18.12^{+0.15}_{-0.12}$	$18.19^{+0.15}_{-0.13}$
UrsaMinor	$18.47^{+0.13}_{-0.09}$	$18.46^{+0.09}_{-0.08}$	$18.50^{+0.09}_{-0.08}$	$18.46^{+0.09}_{-0.08}$	$18.46^{+0.08}_{-0.07}$	$18.47^{+0.09}_{-0.08}$

Figure 4 shows that introducing R dependence in the likelihood function mitigates the degeneracy between ρ_s and r_s in SA20. Since certain combinations of ρ_s and r_s give the same value of mean $\sigma^2_{\rm los}$, R-independent likelihood as used in SA20 has a degeneracy problem. In contrast, the function $\sigma^2_{\rm los}$ is not equivalent even for such a combination, hence it allows us to distinguish these parameter sets. Introducing R dependence however causes another issue, namely, arbitrariness of anisotropy function $\beta(r)$, which is just assumed to be constant for simplicity in this study. In order to remove unexpected bias, this arbitrariness should be carefully treated in the further study as well as other arbitrariness such as the axisymmetricity.

B. J factor and Bayes factor

Figure 5 shows that, in the satellite prior only analysis, our estimates of log-J factor are larger by $\sim\mathcal{O}(0.1)$ than those estimated in SA20. This is because the R dependence of our likelihood function weakens the ρ_s-r_s degeneracy, as mentioned in the previous section, and excludes the too compact (small r_s, large ρ_s) or faint (large r_s, small ρ_s) dark matter halo with small J-factor value.

Figure 5 also shows that SHMR priors decrease the uncertainty of J factor by up to about 50%, but estimated median values have SHMR model dependence and some estimations are not consistent with each other. For instance, the PB13 prior tends to predict smaller J factor than other priors for dSphs with large J factors such as Segue 1. Conversely, the BM18 prior gives larger J factor than other priors for small J-factor dSphs such as Leo 4. These features come from the difference of SHMR models. As shown in Fig. 2, SHMR models have different slopes for the small M_h region around the mass scale of dSph halos. In particular, the PB13 model has a large m_*/M_h ratio, while the BM18 one has a smaller m_*/M_h than others. Once m_* is fixed by observations, large m_*/M_h gives small M_h, and vice versa. We note that Ref. [74] reported $M/L \sim 1.6$, thus our estimates of stellar mass obtained by assuming $M/L = 1$ are potentially smaller than actual values. However, this discrepancy has no significant effect on our estimation because of the scatter of SHMR models.

Bayes factors help us understand the model dependence of the estimated J factors. Tables IV and VI show that models whose estimate is deviated from the result of satellite prior only analysis tend to have small Bayes factors. For instance, the PB13 model shows $\ln \mathrm{BF} \lesssim -3$ for Segue 1 and Willman 1, and the BM18 shows $\ln \mathrm{BF} \lesssim -1$ for Leo 4. It means that, in terms of the Bayesian analysis, the results of PB13 for Segue 1 and Willman 1 are very strongly less reliable than those of the satellite prior only analysis, and the results of BM18 for Leo 4 are substantially less reliable, respectively. We can understand this feature through posteriors in Fig. 9–12. For these dSphs, posteriors obtained by PB13 or BM18 are significantly deviated from the contour of the satellite prior only analysis, which means that these SHMR models and the satellite prior are incompatible. In contrast, models having comparable J factors to the satellite prior only analysis have Bayes factors almost equal to or larger than the satellite prior only analysis. This tendency of the Bayes factors indicates that the estimated J-factor values with the satellite prior only analysis are stable even when considering SHMRs.

We can utilize this tendency in the opposite direction; not evaluating dark matter profiles by using SHMRs, but evaluating SHMRs by using dark matter profiles. The relation between J factors and Bayes factors suggest some possibilities that there are some unknown biases in the observation of these dSphs or that some SHMR models having small Bayes factors are invalid for certain ultrafaint dSphs. The latter possibility could originate from the difference of the construction of these models; the PB13 model predicts larger m_*/M_h values than the others around the small halo mass region, while those of the BM18 model are smaller than the others (see Fig. 2). In particular, Ref. [63] indicated that PB13 assumed a strong surface-brightness incompleteness correction for faint galaxies that

FIG. 5. Estimated J factors of ultrafaint dwarf spheroidal galaxies in Table IV (dots) and their 68% credible intervals (error bars). The black bars are the results with satellite prior only analysis, while the gray ones show the results of conventional analysis [11]. The blue, orange, green and red bars correspond to analyses with the satellite prior and PB13, BM13, PB19 and BM18 priors, respectively. The bars on the white background area correspond to the results for $V_{50} = 10.5$ km/s, while those on the gray-shaded area correspond to the results for $V_{50} = 18$ km/s. The brown bars between white and shaded areas denote the J-factor values used in the Fermi-LAT analysis of the indirect dark matter search [73].

is no longer observationally supported [75], which causes the overestimate of the SHMR around the low halo mass region. For BM18, Ref. [64] pointed out that the underestimate of the BM18 model around the low-halo mass region occurs to compensate the overestimation of the number of massive galaxies caused by the Eddington bias. Further investigation of these features would help us to improve and calibrate these SHMR models using dSph observation or reveal some unknown nature of dSphs.

Since the J-factor values of the ultrafaint dSphs obtained in this work are not significantly different from conventional values, there are no significant updates for the current dark matter constraints of the indirect detection experiment. The detection sensitivity depends on the lower bounds of J factors. Because J factors of dSphs with the largest J factors such as Segue 1 and Ursa Major 2 do not change significantly even when considering cosmological priors having largest Bayes factors, constraints on dark matter parameters do also not show significant difference. The constraints however could be updated when we select only a part of dSphs as detection targets, where the J factor lower bound of each dSph matters.

In contrast, from Table V and Fig. 6, the J-factor uncertainty of classical dSphs obtained in this work is reduced up to about 20% of the results of SA20 due to the consideration of R dependence of the velocity dispersion.

TABLE VI. The natural logarithm of Bayes factors of each model calculated according to Eq. (22). Column 1 shows the Bayes factor of sat_{18} to a reference model $\mathrm{sat}_{10.5}$ for each dSph. Columns 2–5 show the Bayes factors of the satellite prior and SHMR analyses to the satellite prior only analysis $\mathrm{sat}_{10.5}$ as a reference, so as columns 6–9 not for $\mathrm{sat}_{10.5}$ but sat_{18} cases. By definition, positive (negative) values mean that the corresponding model is more (less) credible than the reference model.

	$\mathrm{sat}_{18}/\mathrm{sat}_{10.5}$	$(\mathrm{sat}_{10.5}+\mathrm{SHMR})/\mathrm{sat}_{10.5}$				$(\mathrm{sat}_{18}+\mathrm{SHMR})/\mathrm{sat}_{18}$			
Name	w/o SHMR	PB13	BM13	PB19	BM18	PB13	BM13	PB19	BM18
Aquarius2	0.77	−1.16	0.17	0.34	1.13	−2.16	−0.35	0.05	0.29
Bootes1	−0.01	0.34	0.20	0.17	0.09	0.12	0.10	0.21	0.11
Bootes2	−0.09	0.05	0.06	−0.05	−0.16	0.07	0.04	0.01	−0.01
CanesVenatici1	0.49	0.36	0.49	0.07	0.34	0.33	−0.01	−0.31	−0.03
CanesVenatici2	1.29	−0.70	0.64	0.92	2.08	−2.61	−0.70	0.15	0.71
Carina2	−0.14	0.65	0.44	0.03	−0.35	0.76	0.30	0.29	−0.19
ComaBerenices	1.06	−1.71	−0.09	0.35	1.75	−3.07	−0.52	0.07	0.64
Draco2	0.16	0.10	0.10	0.04	0.24	−0.07	−0.09	−0.05	−0.01
Eridanus2	0.79	−0.22	0.76	0.94	1.53	−0.62	−0.03	0.05	0.78
Grus1	−0.30	0.34	0.14	−0.07	−0.40	0.27	0.19	0.10	−0.07
Hercules	0.88	0.58	0.96	0.59	1.06	−0.04	−0.06	−0.07	0.15
Horologium1	1.12	−3.87	−0.78	−0.44	1.25	−4.13	−0.58	−0.03	0.25
Hydrus1	−0.17	0.30	0.23	−0.20	−0.89	0.38	0.09	−0.03	−0.85
Leo4	−0.16	0.34	0.02	−0.05	−0.93	0.44	0.15	0.01	−0.72
Leo5	−0.03	0.34	0.51	0.04	0.24	−0.47	−0.15	0.31	0.45
LeoT	1.39	0.65	1.85	1.43	0.84	−0.01	0.47	0.08	−0.61
Pegasus3	1.28	−0.19	0.37	0.11	1.62	−1.65	−0.98	−0.06	0.25
Pisces2	0.27	0.49	0.26	−0.04	−0.07	0.29	−0.01	−0.11	−0.28
Reticulum2	0.96	−1.08	0.03	0.17	1.13	−1.85	−0.82	−0.12	0.13
Segue1	1.89	−2.63	−1.00	−0.27	1.36	−4.29	−1.01	−0.05	−0.41
Segue2	0.08	0.11	0.12	0.21	0.26	−0.17	−0.20	0.04	−0.10
Triangulum2	−0.65	−0.01	0.14	−0.02	−0.52	0.57	0.37	0.08	0.16
Tucana2	−0.13	−0.23	0.16	0.11	−0.09	−0.54	0.12	0.16	−0.06
Tucana3	−2.75	0.56	0.18	−0.01	−2.82	3.39	2.68	−0.08	0.08
UrsaMajor1	1.06	−5.26	−0.16	0.61	1.84	−5.30	−0.45	−0.08	0.80
UrsaMajor2	1.25	−4.98	−1.11	0.05	1.67	−5.93	−0.63	−0.21	0.37
Willman1	2.07	−3.05	−1.05	−0.62	1.71	−4.90	−1.26	−0.37	−0.29

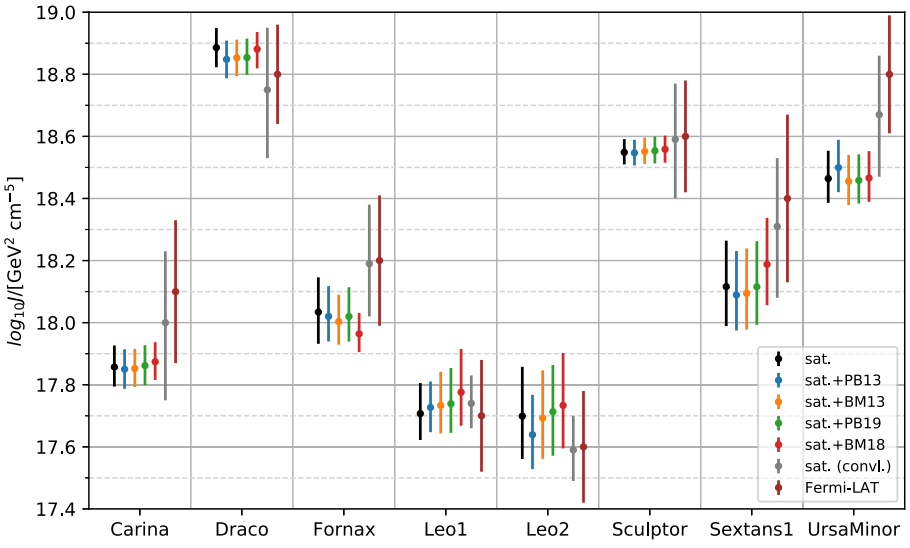

FIG. 6. Same as Fig. 5 but for the classical dSphs listed in Table V.

In particular, the Draco dSph, having one of the largest J factors, has larger lower bound by about 0.25 in logarithmic scale than SA20. Since indirect detection sensitivity reflects the lower bound of the J factor, the sensitivity might be stronger than the results of SA20. Here we should note that our results have an implicit bias of dSph model construction. In other conventional works such as Ref. [8] the uncertainty of the dark matter profile is taken into account by introducing more general dark matter profile models and they indicate the deviation of dark matter profile from the simple NFW profile. In this paper, however, we neglect the uncertainty of dark matter profile by fixing it to be the NFW profile and also that of the anisotropy profile by assuming constant model, thus our results have an implicit bias based on the model construction. In order to calculate more reliable J-factor values, we need further investigation to implement the flexibility of the dark matter profile into the cosmological prior analysis.

V. SUMMARY AND CONCLUSION

In this paper, we utilized two cosmological priors (satellite and SHMR) and a likelihood function with radial dependence to obtain better constraints on the dark matter halo profile of dSphs through the kinematical fitting using the spherical Jeans equation. We prepared some different setups for the cosmological priors and estimate the posterior probability density function and J factor. We compared these models and showed that our J-factor estimates obtained by using the satellite prior are stable in terms of their Bayes factors even when considering another cosmological prior, the SHMR prior. Cosmological priors and the R dependence of the likelihood mitigate the degeneracy between parameters and decrease the uncertainty of J-factor values up to about 50% for ultrafaint dSphs and about 20% for classical dSphs. These estimates would be updated by introducing the flexibility of dSph models (e.g., anisotropy, halo profile and nonsphericity).

ACKNOWLEDGMENTS

This research made use of ASTROPY [76] a community-developed core PYTHON package for Astronomy [77,78], NumPy [79], the fundamental package for scientific computing with PYTHON [80], and PANDAS [81], a fast, powerful, flexible and easy to use open source data analysis and manipulation tool, built on top of the PYTHON programming language [82,83]. This work was supported by KAKENHI Grants No. JP20H05850 (S. H. and S. A.), No. JP20H05861 (S. A.), and Japan Society for the Promotion of Science (JSPS) KAKENHI Grants No. JP20H01895, No. JP21K13909, No. JP21H05447 and No. JP23H04009 (K. H.). Kavli Institute for the Physics and Mathematics of the Universe (WPI) is supported by World Premier International Research Centre Initiative (WPI), MEXT, Japan.

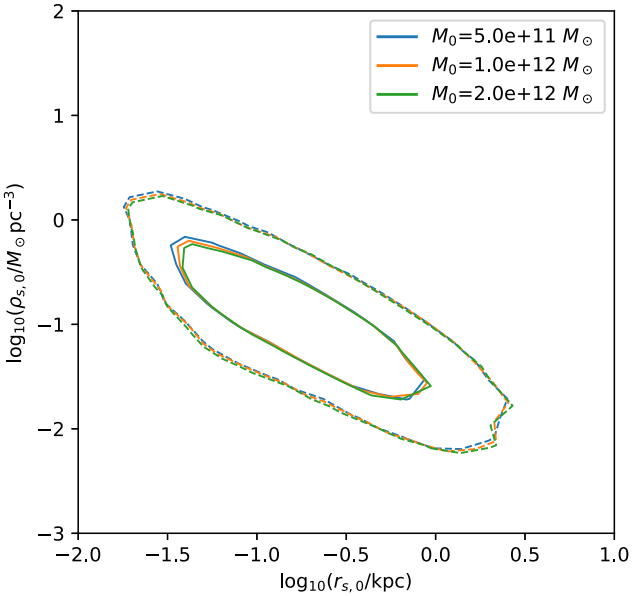

FIG. 7. Satellite priors assuming different Milky Way masses 0.5, 1.0, and $2.0 \times 10^{12} M_\odot$ by the blue, orange, and green lines, respectively.

APPENDIX A: ASSUMPTION ON MILKY WAY

In this study we assume that the Milky Way profile is the NFW profile with mass $10^{12} M_\odot$. In order to investigate the impact of Milky Way models, we calculate the satellite priors $\pi_{\rm sat}$ under different assumptions on the Milky Way mass in Fig. 7. Here we compare the priors whose host halo mass are set to 0.5, 1.0, and $2.0 \times 10^{12} M_\odot$, shown by the blue, orange, and green lines, respectively. The figure shows that Milky Way mass does not affect the prior distribution more than SMHR models as the mass-loss rate [Eq. (13)] only weakly depends on the host halo mass as mentioned in SA20, which allows us to ignore this effect in this study when considering various SHMR models.

APPENDIX B: IMPACT OF SHMR UNCERTAINTY

As SHMR models are mainly calibrated for heavier galaxies than (ultrafaint) dSphs, the actual uncertainty for low-mass galaxies such as (ultrafaint) dSphs could be inaccurate compared with those expected by extrapolation due to the limited available data. In Fig. 8, we demonstrate the impact of model uncertainty levels by setting them to fixed values. The gray lines depict the cosmological priors ($\pi_{\rm sat+SHMR}$) adopted in this study, while the colored lines correspond to those with manually fixed uncertainty level. The light gray lines correspond to the satellite prior without any SHMRs ($\pi_{\rm sat.}$). As shown in the figures, increasing the uncertainty leads to broader probability distributions, as expected by the definition of cosmological priors:

$$\pi_{\rm sat+SHMR} \to \pi_{\rm sat}(\delta \log_{10}(m_*/[M_\odot]) \to \infty). \quad \text{(B1)}$$

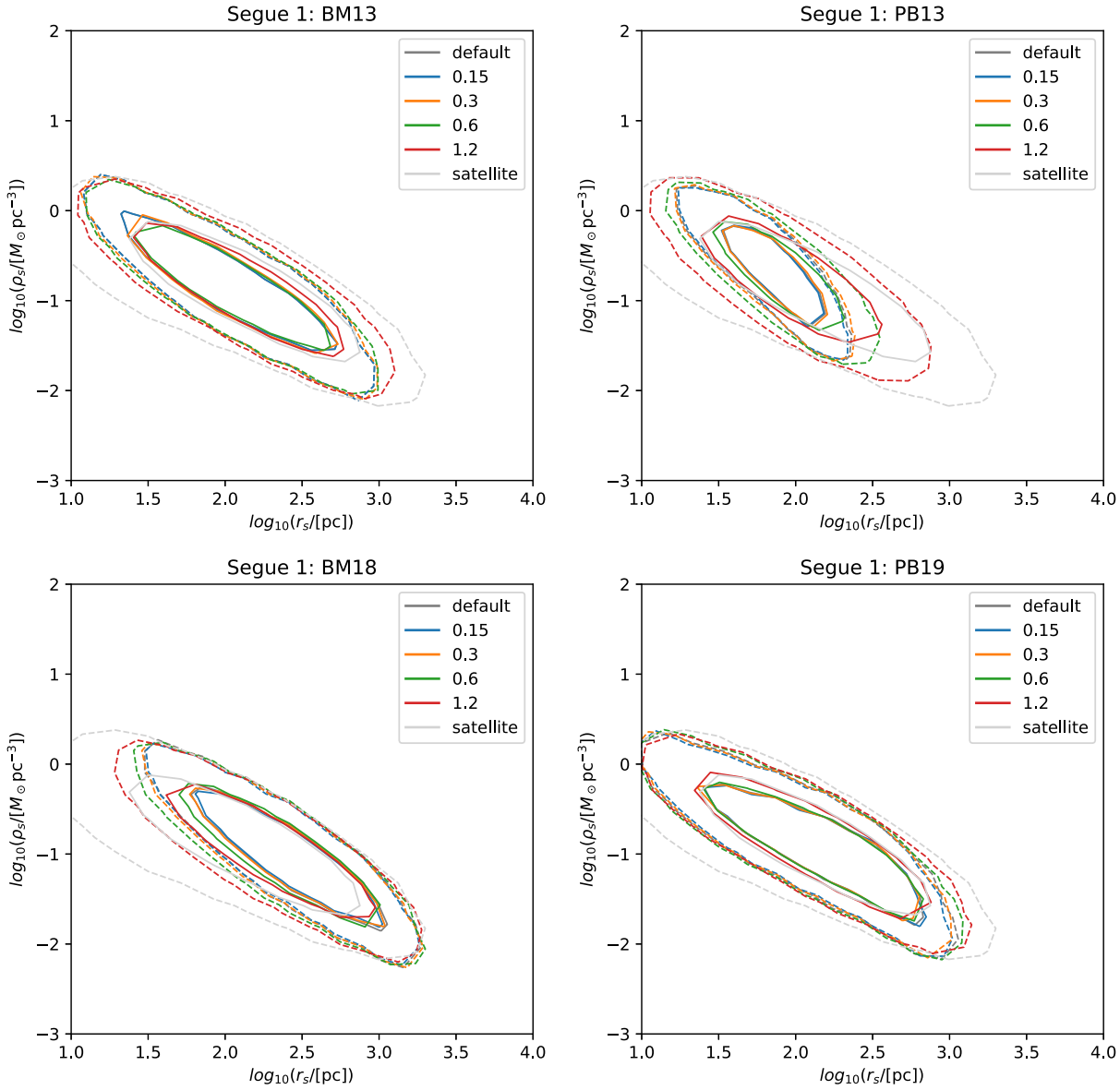

FIG. 8. Probability density distributions of satellite and SHMR priors $\pi_{\rm sat+SHMR}$ are shown with varying levels of uncertainty in each SHRM model. The gray lines depict the distribution with default uncertainties obtained from the literature, while the light gray lines correspond to the satellite prior without any SHMRs ($\pi_{\rm sat.}$). The colored (blue, orange, green, and red) lines represent the probability density distributions with manually fixed uncertainty levels [$\delta \log_{10}(m_*/[M_\odot]) = 0.15$, 0.3, 0.6, and 1.25, respectively].

Therefore, even when the actual uncertainty of SHMR models is larger than those expected by extrapolation and the prior $\pi_{\rm sat+SHMR}$ could be inaccurate, our analysis using $\pi_{\rm sat}$ gives robust estimation of J factors.

APPENDIX C: POSTERIORS

Posterior probability density distribution projected onto the r_s-ρ_s plane are shown in Fig. 9–13. Here Fig. 9–12 are for ultrafaint dSphs, while Fig. 13 is for classical dSphs.

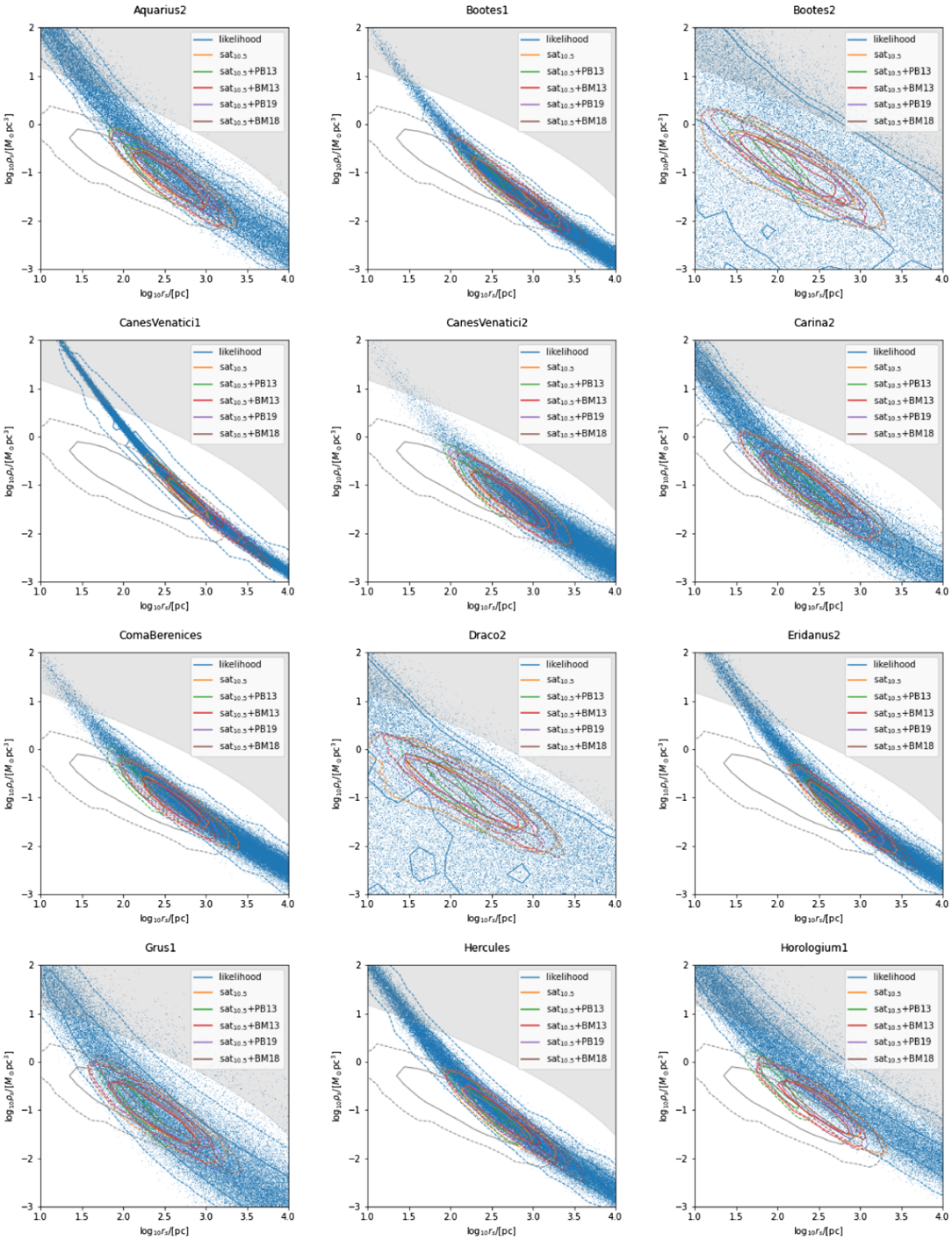

FIG. 9. Posterior probability density distribution projected onto the r_s-ρ_s plane with $\mathrm{sat}_{10.5}$ prior. The gray shaded area shows the cosmological constraint adopted in Ref. [8]. The gray contours show the probability density distribution of the satellite prior $\mathrm{sat}_{10.5}$. The blue dots and contours illustrate the shape of the likelihood function (flat prior). Colored contours show the posterior probability density distribution assuming our cosmological priors.

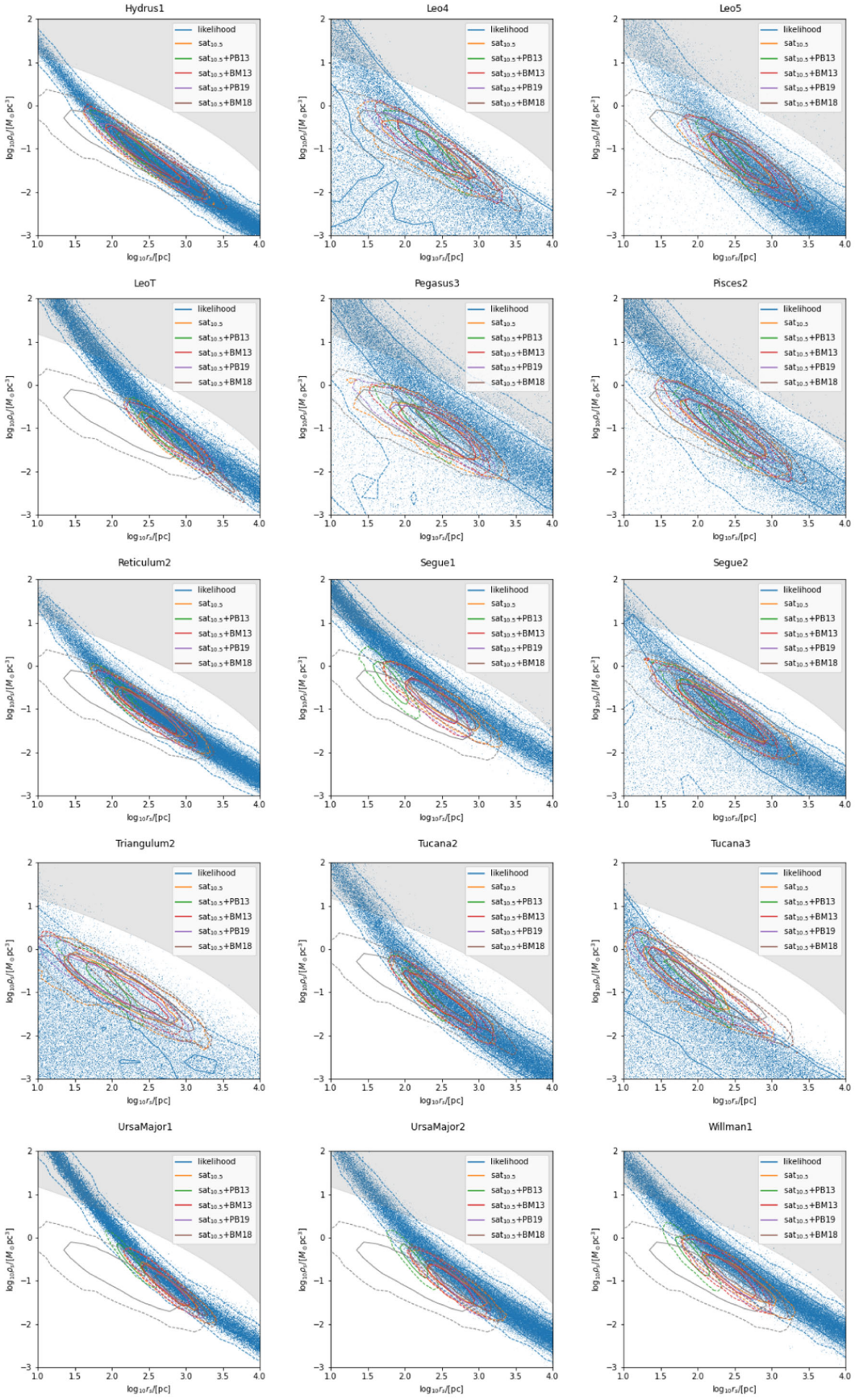

FIG. 10. This is continued from Fig. 9.

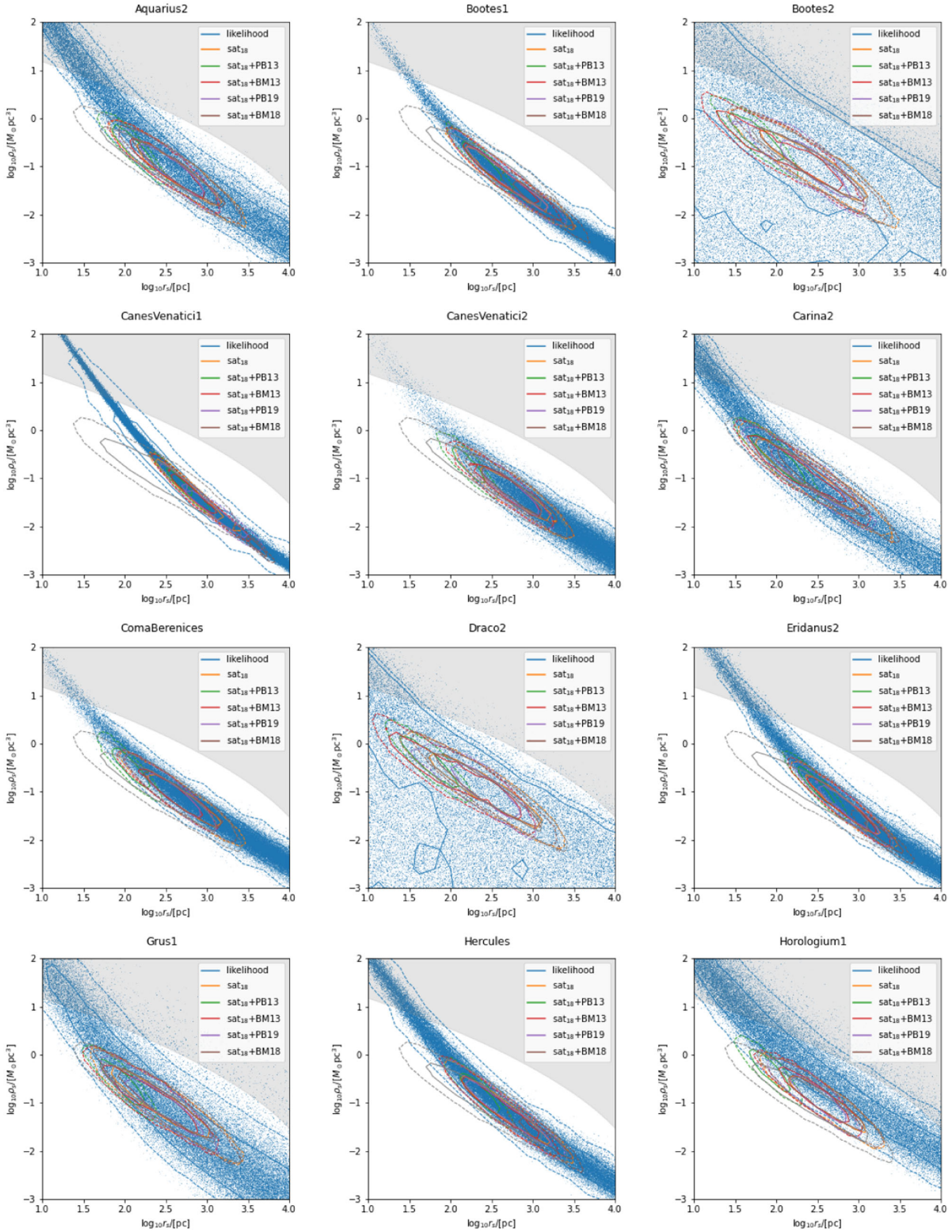

FIG. 11. This is the same figure as Fig. 9 but using the satellite prior sat_{18}.

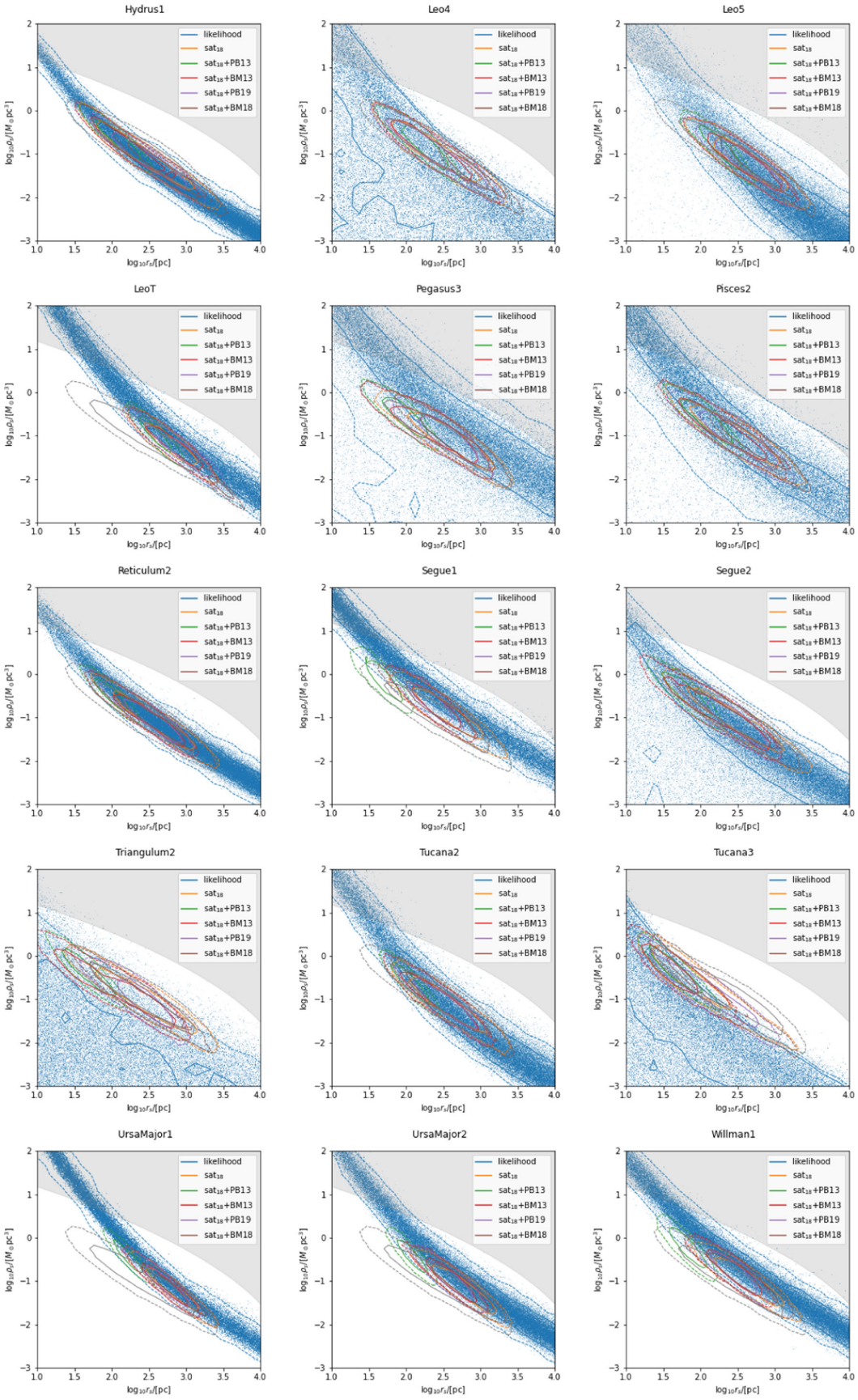

FIG. 12. This is continued from Fig. 11.

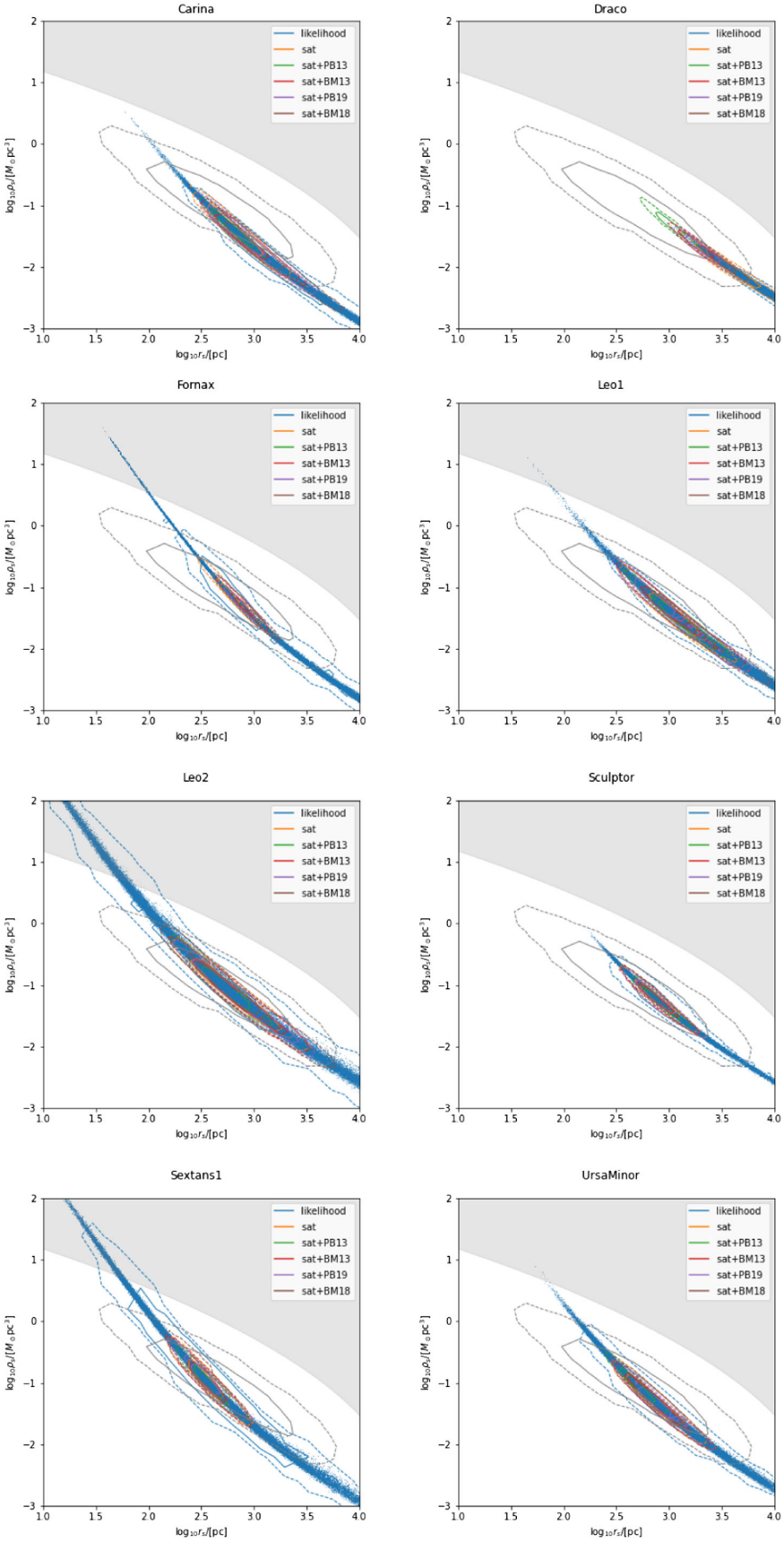

FIG. 13. This is the same as Fig. 9–12 but for classical dSphs.

[1] N. Aghanim *et al.* (Planck Collaboration), Astron. Astrophys. **641**, A6 (2020); **652**, C4(E) (2021).
[2] J. L. Feng, Annu. Rev. Astron. Astrophys. **48**, 495 (2010).
[3] B. Bhattacherjee, M. Ibe, K. Ichikawa, S. Matsumoto, and K. Nishiyama, J. High Energy Phys. 07 (2014) 080.
[4] S. Ando and K. Ishiwata, Phys. Rev. D **104**, 023016 (2021).
[5] J. Hisano, S. Matsumoto, and M. M. Nojiri, Phys. Rev. Lett. **92**, 031303 (2004).
[6] J. Hisano, S. Matsumoto, M. M. Nojiri, and O. Saito, Phys. Rev. D **71**, 063528 (2005).
[7] J. Binney and S. Tremaine, *Galactic Dynamics*, 2nd ed. (Princeton University Press, Princeton, New Jersey, 1987).
[8] A. Geringer-Sameth, S. M. Koushiappas, and M. Walker, Astrophys. J. **801**, 74 (2015).
[9] N. Hiroshima, S. Ando, and T. Ishiyama, Phys. Rev. D **97**, 123002 (2018).
[10] S. Ando, T. Ishiyama, and N. Hiroshima, Galaxies **7**, 68 (2019).
[11] S. Ando, A. Geringer-Sameth, N. Hiroshima, S. Hoof, R. Trotta, and M. G. Walker, Phys. Rev. D **102**, 061302 (2020).
[12] J. F. Navarro, C. S. Frenk, and S. D. M. White, Astrophys. J. **490**, 493 (1997).
[13] R. H. Wechsler and J. L. Tinker, Annu. Rev. Astron. Astrophys. **56**, 435 (2018).
[14] The sphericity of dSphs is also assumed when deriving the satellite prior [11]. However, Ref. [15] suggests that axisymmetric models show better fitting performance than spherical models in terms of Bayes factor comparison. Hence, further study on the axisymmetric formalization of the satellite prior would be useful for future J-factor analyses, which is however beyond the scope of this paper.
[15] K. Hayashi, K. Ichikawa, S. Matsumoto, M. Ibe, M. N. Ishigaki, and H. Sugai, Mon. Not. R. Astron. Soc. **461**, 2914 (2016).
[16] V. Bonnivard *et al.*, Mon. Not. R. Astron. Soc. **453**, 849 (2015).
[17] H. C. Plummer, Mon. Not. R. Astron. Soc. **71**, 460 (1911).
[18] Note that the stellar profile fitting by using a generalized function suggests that some dSphs have multiple components [19,20].
[19] K. Hayashi, M. Fabrizio, E. L. Łokas, G. Bono, M. Monelli, M. Dall'Ora, and P. B. Stetson, Mon. Not. R. Astron. Soc. **481**, 250 (2018).
[20] A. B. Pace, M. Kaplinghat, E. Kirby, J. D. Simon, E. Tollerud, R. R. Muñoz, P. Côté, S. G. Djorgovski, and M. Geha, Mon. Not. R. Astron. Soc. **495**, 3022 (2020).
[21] W. J. G. de Blok, Adv. Astron. **2010**, 789293 (2010).
[22] G. A. Mamon and E. L. Łokas, Mon. Not. R. Astron. Soc. **363**, 705 (2005).
[23] In SA20 they assume the normal distribution for the half-light radius, but we found no significant difference between the normal and log-normal distributions because the standard deviation is so small that the log-normal distribution can be approximated by the normal distribution. In this paper, we adopt log-normal distribution, reflecting the fact that the radius must be positive.
[24] A. W. McConnachie, Astron. J. **144**, 4 (2012).
[25] G. Torrealba, S. E. Koposov, V. Belokurov, M. Irwin, M. Collins, M. Spencer, R. Ibata, M. Mateo, A. Bonaca, and P. Jethwa, Mon. Not. R. Astron. Soc. **463**, 712 (2016).
[26] S. E. Koposov, G. Gilmore, M. G. Walker, V. Belokurov, N. W. Evans, M. Fellhauer, W. Gieren, D. Geisler, L. Monaco, J. E. Norris, S. Okamoto, J. Peñarrubia, M. Wilkinson, R. F. G. Wyse, and D. B. Zucker, Astrophys. J. **736**, 146 (2011).
[27] A. Koch, M. I. Wilkinson, J. T. Kleyna, M. Irwin, D. B. Zucker, V. Belokurov, G. F. Gilmore, M. Fellhauer, and N. W. Evans, Astrophys. J. **690**, 453 (2009).
[28] A. P. Ji, A. Frebel, J. D. Simon, and M. Geha, Astrophys. J. **817**, 41 (2016).
[29] J. D. Simon and M. Geha, Astrophys. J. **670**, 313 (2007).
[30] T. S. Li *et al.* (MagLiteS Collaboration), Astrophys. J. **857**, 145 (2018).
[31] N. F. Martin, M. Geha, R. A. Ibata, M. L. M. Collins, B. P. M. Laevens, E. F. Bell, H.-W. Rix, A. M. N. Ferguson, K. C. Chambers, R. J. Wainscoat, and C. Waters, Mon. Not. R. Astron. Soc. **458**, L59 (2016).
[32] T. S. Li *et al.* (DES Collaboration), Astrophys. J. **838**, 8 (2017).
[33] M. G. Walker, M. Mateo, E. W. Olszewski, S. Koposov, V. Belokurov, P. Jethwa, D. L. Nidever, V. Bonnivard, I. Bailey, John I., E. F. Bell, and S. R. Loebman, Astrophys. J. **819**, 53 (2016).
[34] S. E. Koposov *et al.*, Astrophys. J. **811**, 62 (2015).
[35] S. E. Koposov, M. G. Walker, V. Belokurov, A. R. Casey, A. Geringer-Sameth, D. Mackey, G. Da Costa, D. Erkal, P. Jethwa, M. Mateo, E. W. Olszewski, and J. I. Bailey, Mon. Not. R. Astron. Soc. **479**, 5343 (2018).
[36] S. A. Jenkins, T. S. Li, A. B. Pace, A. P. Ji, S. E. Koposov, and B. Mutlu-Pakdil, Astrophys. J. **920**, 92 (2021).
[37] D. Kim, H. Jerjen, M. Geha, A. Chiti, A. P. Milone, G. Da Costa, D. Mackey, A. Frebel, and B. Conn, Astrophys. J. **833**, 16 (2016).
[38] E. N. Kirby, J. D. Simon, and J. G. Cohen, Astrophys. J. **810**, 56 (2015).
[39] J. D. Simon *et al.* (DES Collaboration), Astrophys. J. **808**, 95 (2015).
[40] J. D. Simon, M. Geha, Q. E. Minor, G. D. Martinez, E. N. Kirby, J. S. Bullock, M. Kaplinghat, L. E. Strigari, B. Willman, P. I. Choi, E. J. Tollerud, and J. Wolf, Astrophys. J. **733**, 46 (2011).
[41] E. N. Kirby, M. Boylan-Kolchin, J. G. Cohen, M. Geha, J. S. Bullock, and M. Kaplinghat, Astrophys. J. **770**, 16 (2013).
[42] E. N. Kirby, J. G. Cohen, J. D. Simon, P. Guhathakurta, A. O. Thygesen, and G. E. Duggan, Astrophys. J. **838**, 83 (2017).
[43] J. D. Simon *et al.* (DES Collaboration), Astrophys. J. **838**, 11 (2017).
[44] B. Willman, M. Geha, J. Strader, L. E. Strigari, J. D. Simon, E. Kirby, N. Ho, and A. Warres, Astron. J. **142**, 128 (2011).
[45] X. Yang, H. J. Mo, Y. Zhang, and F. C. van den Bosch, Astrophys. J. **741**, 13 (2011).
[46] C. A. Correa, J. S. B. Wyithe, J. Schaye, and A. R. Duffy, Mon. Not. R. Astron. Soc. **452**, 1217 (2015).
[47] T. Ishiyama, S. Rieder, J. Makino, S. Portegies Zwart, D. Groen, K. Nitadori, C. de Laat, S. McMillan, K. Hiraki, and S. Harfst, Astrophys. J. **767**, 146 (2013).
[48] F. Jiang and F. C. van den Bosch, Mon. Not. R. Astron. Soc. **458**, 2848 (2016).
[49] Here we assume that there is no correlation between (m_a, z_a) and $c_{t,a}$.

[50] S. Ando, N. Hiroshima, and A. Dekker, SASHIMI-C: Semi-Analytical SubHalo Inference ModelIng for Cold Dark Matter [Computer software] (2023), https://github.com/shinichiroando/dwarf_params.
[51] G. Efstathiou, Mon. Not. R. Astron. Soc. **256**, 43P (1992).
[52] A. S. Graus, J. S. Bullock, T. Kelley, M. Boylan-Kolchin, S. Garrison-Kimmel, and Y. Qi, Mon. Not. R. Astron. Soc. **488**, 4585 (2019).
[53] A. A. Thoul and D. H. Weinberg, Astrophys. J. **465**, 608 (1996).
[54] N. Y. Gnedin, Astrophys. J. **542**, 535 (2000).
[55] M. Hoeft, G. Yepes, S. Gottlöber, and V. Springel, Mon. Not. R. Astron. Soc. **371**, 401 (2006).
[56] T. Okamoto, L. Gao, and T. Theuns, Mon. Not. R. Astron. Soc. **390**, 920 (2008).
[57] J. R. Hargis, B. Willman, and A. H. G. Peter, Astrophys. J. Lett. **795**, L13 (2014).
[58] P. Virtanen *et al.* (SciPy 1.0 Contributors), Nat. Methods **17**, 261 (2020).
[59] R. H. Wechsler and J. L. Tinker, Annu. Rev. Astron. Astrophys. **56**, 435 (2018).
[60] Basically, a galaxy is hosted at the center of a dark matter halo which is more massive than stellar mass, and the tidal force strips mainly the dominant component of the halo mass. Therefore stellar mass is not significantly changed until most of the halo mass is striped and halo mass and galaxy mass become comparable. However, once the halo mass becomes comparable, it cannot bound the galaxy within the halo and the galaxy gets collapsed, thus we cannot find such galaxies anymore.
[61] P. S. Behroozi, R. H. Wechsler, and C. Conroy, Astrophys. J. **770**, 57 (2013).
[62] B. P. Moster, T. Naab, and S. D. M. White, Mon. Not. R. Astron. Soc. **428**, 3121 (2013).
[63] P. Behroozi, R. H. Wechsler, A. P. Hearin, and C. Conroy, Mon. Not. R. Astron. Soc. **488**, 3143 (2019).
[64] B. P. Moster, T. Naab, and S. D. M. White, Mon. Not. R. Astron. Soc. **477**, 1822 (2018).
[65] S. Watanabe, J. Mach. Learn. Res. **14**, 867 (2012).
[66] H. Jeffreys, *The Theory of Probability*, Oxford Classic Texts in the Physical Sciences (Oxford University Press, Oxford, 1939).
[67] M. G. Walker, M. Mateo, and E. W. Olszewski, Astron. J. **137**, 3100 (2009).
[68] M. G. Walker, E. W. Olszewski, and M. Mateo, Mon. Not. R. Astron. Soc. **448**, 2717 (2015).
[69] M. Mateo, E. W. Olszewski, and M. G. Walker, Astrophys. J. **675**, 201 (2008).
[70] M. E. Spencer, M. Mateo, M. G. Walker, and E. W. Olszewski, Astrophys. J. **836**, 202 (2017).
[71] M. E. Spencer, M. Mateo, E. W. Olszewski, M. G. Walker, A. W. McConnachie, and E. N. Kirby, Astron. J. **156**, 257 (2018).
[72] D. Foreman-Mackey, D. W. Hogg, D. Lang, and J. Goodman, Publ. Astron. Soc. Pac. **125**, 306 (2013).
[73] M. Ackermann *et al.* (Fermi-LAT Collaboration), Phys. Rev. Lett. **115**, 231301 (2015).
[74] J. Woo, S. Courteau, and A. Dekel, Mon. Not. R. Astron. Soc. **390**, 1453 (2008).
[75] R. P. Williams, I. K. Baldry, L. S. Kelvin, P. A. James, S. P. Driver, M. Prescott, S. Brough, M. J. I. Brown, L. J. M. Davies, B. W. Holwerda, J. Liske, P. Norberg, A. J. Moffett, and A. H. Wright, Mon. Not. R. Astron. Soc. **463**, 2746 (2016).
[76] http://www.astropy.org.
[77] T. P. Robitaille *et al.* (Astropy Collaboration), Astron. Astrophys. **558**, A33 (2013).
[78] A. M. Price-Whelan *et al.* (Astropy Collaboration), Astron. J. **156**, 123 (2018).
[79] https://numpy.org/.
[80] C. R. Harris *et al.*, Nature (London) **585**, 357 (2020).
[81] https://pandas.pydata.org/.
[82] Pandas development team, pandas-dev/pandas: Pandas 1.2.4 (2021), https://github.com/pandas-dev/pandas.
[83] Wes McKinney, in *Proceedings of the 9th PYTHON in Science Conference*, edited by Stéfan van der Walt and Jarrod Millman (2010), pp. 56–61, 10.25080/Majora-92bf1922-00a.